

PIVOTS: Aligning unseen Structures using Preoperative to Intraoperative Volume-To-Surface Registration for Liver Navigation

Peng Liu^{a,b,c,d,1,*}, Bianca Güttner^{a,b,c,d,1}, Yutong Su^{a,b,c,d}, Chenyang Li^{a,b,c,d}, Jinjing Xu^{a,b,c,d}, Mingyang Liu^g, Zhe Min^g, Andrey Zhylka^h, Jasper Smit^h, Karin Olthof^h, Matteo Fusaglia^h, Rudi Apolle^{i,c,b,1}, Matthias Miederer^{i,c,b,1}, Laura Frohneberger^c, Carina Riediger^c, Jürgen Weitz^c, Fiona Kolbinger^{e,j}, Stefanie Speidel^{a,b,c,d,f}, Micha Pfeiffer^{a,b,c,d}

^aTranslational Surgical Oncology, National Center for Tumor Diseases, Fetscherstrasse 74/PF 64, Dresden, 01307, Saxony, Germany

^bGerman Cancer Research Center (DKFZ), Im Neuenheimer Feld 280, Heidelberg, 69120, Baden-Württemberg, Germany

^cFaculty of Medicine and University Hospital Carl Gustav Carus, Dresden, 01307, Saxony, Germany

^dHelmholtz-Zentrum Dresden-Rossendorf (HZDR), Dresden, Saxony, Germany

^eDepartment of Visceral, Thoracic and Vascular Surgery, University Hospital and Faculty of Medicine Carl Gustav Carus, TUD Dresden University of Technology, Dresden, 01307, Saxony, Germany

^fCentre for Tactile Internet with Human-in-the-Loop, TU Dresden, Dresden, Saxony, Germany

^gSchool of Control Science and Engineering, Shandong University, Jinan, Shandong, China

^hSurgical Department, The Netherlands Cancer Institute, Amsterdam, Netherlands

ⁱTranslational Imaging in Oncology, National Center for Tumor Diseases, Fetscherstrasse 74/PF 64, Dresden, 01307, Saxony, Germany

^jWeldon School of Biomedical Engineering, Purdue University, West Lafayette, IN, USA

Abstract

Non-rigid registration is essential for Augmented Reality guided laparoscopic liver surgery by fusing preoperative information, such as tumor location and vascular structures, into the limited intraoperative view, thereby enhancing surgical navigation. A prerequisite is the accurate prediction of intraoperative liver deformation which remains highly challenging due to factors such as large deformation caused by pneumoperitoneum, respiration and tool interaction as well as noisy intraoperative data, and limited field of view due to occlusion and constrained camera movement. To address these challenges, we introduce **PIVOTS**, a **P**reoperative to **I**ntraoperative **V**olume-**T**o-**S**urface registration neural network that directly takes point clouds as input for deformation prediction. The geometric feature extraction encoder allows multi-resolution feature extraction, and the decoder, comprising novel deformation aware cross attention modules, enables pre- and intraoperative information interaction and accurate multi-level displacement prediction. We train the neural network on synthetic data simulated from a biomechanical simulation pipeline and validate its performance on both synthetic and real datasets. Results demonstrate superior registration performance of our method compared to baseline methods, exhibiting strong robustness against high amounts of noise, large deformation, and various levels of intraoperative visibility. We publish the training and test sets as evaluation benchmarks and call for a fair comparison of liver registration methods with volume-to-surface data. Code and datasets are available here <https://github.com/pengliu-nct/PIVOTS>.

Keywords: Intraoperative, Liver Navigation, Point Clouds, Nonrigid, Registration, Volume-to-surface

1. Introduction

Laparoscopic liver surgery (LLS) is a minimally invasive approach for hepatic resection that utilizes small abdominal incisions, specialized instruments, and high-resolution camera systems. During LLS, surgeons strategically insert trocars into the abdominal cavity, through which they introduce surgical instruments and a laparoscope for real-time imaging, allowing them to navigate and resect the targeted liver tissue. Compared to open surgery, LLS offers decreased blood loss, postoperative pain and infectious complications, shorter hospital stays, and faster recovery, while matching the oncological results with respect to margin accuracy and recurrence rates (Novitsky et al.,

2004; Abu Hilal et al., 2018; Amodu et al., 2022; Nguyen et al., 2011; Ratti et al., 2018).

Despite these advantages, such minimally invasive procedures also introduce multiple challenges. Intraoperative views only show the tissue surface that presents scarce distinct texture features, are often restricted by occlusions from adjacent tissues or instruments and confined operating spaces, and additionally degraded by camera artifacts and light reflections. At the same time, preoperative MRI or CT scans provide a comprehensive overview of the abdominal anatomy, detailing critical internal anatomical structures, such as vessels and tumors. Each patient presents a different setting due to morphological variations (Singh and Rabi, 2019; Srimani and Saha, 2020; Santhosh et al., 2024) or due to large tumors distorting the natural shape of the organ. Besides instrument interaction, during surgery, the liver undergoes significant deformation due to respiratory motion, cardiac pulsation, pneumoperitoneum pressure, the round

*Corresponding author. Email: peng.liu@nct-dresden.de

¹These authors contributed equally to this work.

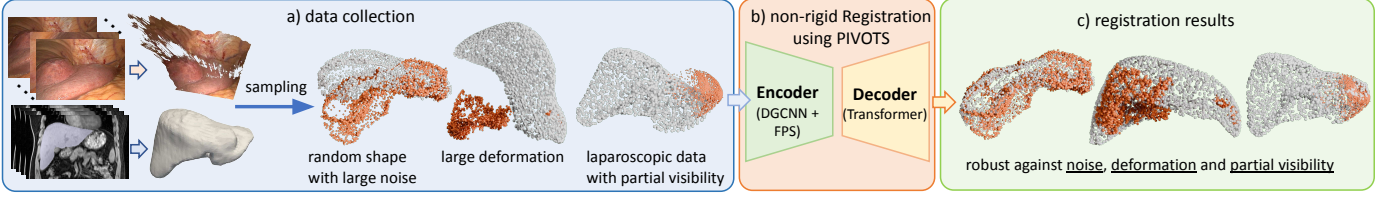


Figure 1: Registration with our method. First, the intraoperative surface (orange) is reconstructed from laparoscopic video and the preoperative volume (gray) is segmented from MRI, and the surface and volume are subsampled as point clouds, depicted in a). These point clouds are then fed into PIVOTS for deformation prediction in b). Finally, the registration results in c) show the robustness of PIVOTS against substantial noise, large deformation and partial visibility.

ligament stabilizing the left lobe and contact with other organs. The tissue properties of a patient’s liver, e.g. stiffness, are unknown prior to surgery while they hold a big influence on the intraoperative deformation and show great variability across the population and across measurement techniques and conditions (Mattei and Ahluwalia, 2016; Marchesseau et al., 2017; Murad Gutiérrez and Romero Enciso, 2018; Lemine et al., 2024): Healthy liver tissue is soft and pliable with a Young’s modulus below 2.5 kPa, becoming much stiffer with comorbidities like liver cirrhosis or fatty liver disease, with ranges up to 16 kPa in non-invasive elastography. These unknowns and mismatches between the data collection modalities impede the direct transfer of preoperative information to intraoperative settings.

However, accurate information transfer is critical for patient safety, since liver surgery involves complex and variable vascular anatomy (hepatic arteries, portal and hepatic veins) and bile duct anatomy, the identification of which can be challenging, particularly in the limited view setting of LLS. Injuries to these structures can lead to serious complications like bleeding, reduced blood supply to the remaining liver, and, potentially, liver failure. Therefore, image-guided laparoscopic navigation systems with augmented reality (AR) are designed to facilitate orientation. Such a navigation system must satisfy several key requirements: It must *i)* ensure an accurate alignment of pre- and intraoperative structures, reliably identifying the visible surface part, *ii)* infer a precise, detailed and sufficiently smooth online deformation of critical structures (such as vessels and small metastases) from the visible parts of the organ, *iii)* demonstrate a high robustness against intraoperative conditions like noise and require *iv)* limited manual intervention while *v)* running on available hardware at very high speeds. To meet these demands, a navigation system must rely on a registration algorithm that is both precise and computationally efficient.

3D-3D registration methods utilize the preoperative liver volume or surface and align it to an intraoperative 3D surface. This intraoperative target surface can be constructed using various methods, such as *Structure from Motion* (SfM) or *Simultaneous Localization and Mapping* (SLAM) methods (Docea et al., 2021, 2022) or by tracking the tool tips (Heiselman et al., 2024). Such reconstructed surfaces are typically small with little overlap with the preoperative full liver volume, and are subject to different types of noise compared to the segmented preoperative 3D liver surfaces. Noise properties differ between reconstruction pipelines based on the choice of endoscope, calibration method, segmentation method, error accumulation due to

heating, tracking and mapping method, amongst others. Rigid registration algorithms then aim to find the optimal rigid transformation between the pre- and intraoperative surfaces, which is usually obtained by extracting point features and then identifying correspondences between the two (Yang et al., 2023b). Non-rigid approaches take this initial alignment as input and deform the preoperative liver volume or surface, so that it reflects the intraoperative state and reveals the hidden structures to surgeons via AR (Pfeiffer et al., 2020). However, current 3D-3D non-rigid registration methods suffer from various challenges, including high sensitivity to volume and surface noise, struggle with large deformation, and a scarcity of high-quality training datasets. Therefore, we propose a novel neural network that yields better registration results with higher robustness against substantial noise and different levels of deformation. The network aims to calculate physically accurate liver deformation from partial views of the organ surface while implicitly estimating unknown boundary conditions and tissue properties. The architecture’s full potential is enabled by our creation of synthetic training data that specifically target above challenges and help overcome the data scarcity issue for registration. Our contributions are fourfold:

- We propose the Point-based **Preoperative to Intraoperative Volume to Surface registration (PIVOTS)**, a novel transformer-based neural network for near real-time deformable liver registration.
- We build upon a **soft-tissue simulation pipeline for registration pair creation** to mitigate the common issue of lacking training and evaluation data.
- We curate a high-quality **healthy human liver breathing motion (HHLBM)** dataset, which can be used to benchmark registration methods, filling the gap of a lack of real evaluation data.
- Our **extensive evaluations** show high registration performance, especially strong robustness against substantial amounts of noise, large deformation, and various amounts of intraoperative visibility.

Our paper is organized as follows: we introduce related work in 3D registration in Sec. 2, followed by the elaboration of the proposed non-rigid neural network and synthetic scene generation in Sec. 3. Then we present various evaluation datasets

in Sec. 4.1 and show results of our experiments: A comparison with SOTA methods (Sec. 4.3), detailed studies of sensitivity to different deformation levels (Sec. 4.4) and noise levels (Sec. 4.5), and an intraoperative visibility experiment (Sec. 4.6), followed by a discussion of strengths and remaining limitations of our method.

2. Related Work

Registration algorithms, which are the core component in laparoscopic navigation systems, can be broadly divided into 3D-3D and 3D-2D registration based on the input modalities. State-of-the-art 3D-3D registration methods can be further categorized into two primary types: 1) traditional approaches, and 2) learning-based methods.

Among traditional registration methods, feature-based methods detect keypoints (Sipiran and Bustos, 2011; Streiff et al., 2021; Jin et al., 2024), which are described with either local or global point descriptors (Rusu et al., 2009; Guo et al., 2013; Zhao et al., 2022). Explicit correspondences are then established through feature matching (Rusu et al., 2008; Guo et al., 2013; Rodola et al., 2013), or voting mechanisms for correspondence optimization (Tombari and Di Stefano, 2010; Yang et al., 2023a).

In contrast to methods relying on one-shot correspondence, which are highly dependent on the quality of feature descriptors and computationally expensive, iterative techniques such as ICP (Besl and McKay, 1992) and its variants (e.g. Go-ICP (Yang et al., 2015), non-rigid ICP (Amberg et al., 2007)) optimize both point correspondences and transformation. Another family of methods relies on implicit correspondences, for instance, CPD ((Myronenko and Song, 2010; Hirose, 2022)) models the source point cloud as the centroids of Gaussians with equal isotropic covariance matrices in a Gaussian Mixture Model. Moreover, these methods are often stuck in local minima given erroneous initial alignment, and focus on surface-to-surface registration, ignoring the volumetric nature and biomechanical properties of an organ. Specifically, in the context of liver navigation, a subset of registration methods employs Biomechanical Models for soft-tissue simulation under boundary conditions to infer intraoperative deformation, often using Finite Element Methods (Özgür et al., 2018; Suwelack et al., 2014; Yang et al., 2024). In theory, these methods model material behavior in a physically accurate way. However, in practice they usually require many simplifications which negate this advantage. Furthermore, they are relatively difficult to parallelize, often suffer from long run-times and can have difficulties adapting to larger deformations.

In light of the marked success of deep learning-based methods, data-driven 3D registration enables end-to-end frameworks, offering computational efficiency and robustness. According to different representations of 3D point clouds and deformation, these learning-based methods can be divided into grid-based, graph-based and point-based methods.

Point clouds present challenges for neural networks due to their irregularity, unordered structure, and varying density. Grid-based methods address these challenges by regularizing

point clouds through implicit representation of shape and deformation. Often, the 3D data is converted to the (truncated) signed distance field (SDF), where each voxel encodes the distance to the closest surface or points, with the signs indicating whether the voxel center is located inside or outside of the target volume. In such a way, this format allows straightforward application of 3D convolution kernels while maintaining information about the surface. Methods such as 3DMatch (Zeng et al., 2017) and PerfectMatch (Gojcic et al., 2019) convert local patches into a volumetric representation of truncated distance field and employ a 3D convolutional neural network to learn local descriptors. V2S-Net (Pfeiffer et al., 2020) transforms preoperative liver volume and intraoperative partial surface into SDF and DF, respectively, while Cue-Net (Liu et al., 2024a) integrates user inputs into the voxel grid as auxiliary information to guide the registration. Both train 3D CNN for deformation prediction. Similarly, (Chen et al., 2024) focuses on voxels surrounding the liver volume and surfaces, but uses a transformer architecture to learn deformation. Despite these advances, voxel representation suffers from several limitations, such as reduced flexibility, since all inputs need to be converted to a fixed voxel grid, and high memory consumption, as every voxel is processed regardless of its proximity to the target, and they are prone to aliasing. By contrast, with the advent of robust backbones for point cloud analysis, learning on point clouds directly becomes increasingly efficient. For example, architectures such as PointNet (Qi et al., 2017a), PointNet++ (Qi et al., 2017b), PointTransformer (Zhao et al., 2021), and KP-Conv (Thomas et al., 2019) facilitate the development of point cloud registration (Yang et al., 2023b; Huang et al., 2020; Sarode et al., 2019; Shi et al., 2021; Yew and Lee, 2022; Qin et al., 2023a; Li and Harada, 2022a).

Harnessing PointNet (Qi et al., 2017a) to extract global features, PointNetLK (Aoki et al., 2019) modifies the Lucas & Kanade algorithm with global feature differences for iterative alignment, whereas PCRNet (Sarode et al., 2019) directly concatenates global features of source and target to regress poses. More recently, LiverMatch (Yang et al., 2023b), RegTR (Yew and Lee, 2022), GeoTransformer (Qin et al., 2023a) and Leopard (Li and Harada, 2022a) utilize KPConv (Thomas et al., 2019) for grid-downsampling. Combined with point feature extraction and self- and cross-attention for feature propagation, the final correspondences and registration results are yielded according to various regression designs. LiverMatch (Yang et al., 2023b) computes correspondences using a confidence matrix and the predicted visibility scores of source points to determine the transformation matrix. RegTR (Yew and Lee, 2022) directly regresses the transformed point clouds from the conditioned features via dual MLP decoders. GeoTransformer (Qin et al., 2023a) adopts a local-to-global scheme, where transformation candidates are first generated between patches with conditioned features, then final transformation is the optimal candidate on the global point clouds. Leopard (Li and Harada, 2022a) integrates positional encoding into a two-block transformer architecture to incrementally achieve robust alignment, suitable for both rigid and non-rigid cases. In contrast, NDP (Li and Harada, 2022b) employs positional encoding with progres-

sively increasing frequencies to address non-rigid registration by shifting from stiff and global alignment to soft and local adjustment.

Another family of 3D learning is Graph-based methods, beginning with the introduction of graph convolutional networks (Scarselli et al., 2008) and later incorporating convolutional networks Duvenaud et al. (2015). Dynamic Graph CNN (DGCNN)(Wang et al., 2019) applies dynamic edge convolution to capture both local and global features in point clouds. DeepClosestPoint (Wang and Solomon, 2019) exploits DGCNN to extract local features for correspondence prediction with an attention module, followed by a differentiable SVD layer for transformation calculation. Predator (Huang et al., 2021) first extracts keypoint features using KPConv, then applies dynamic edge convolution and cross-attention to predict an overlap score between the two groups of superpoints, which are decoded into correspondences by a linear decoder. GraphSCNet (Qin et al., 2023b) constructs a deformation graph over the source point cloud and employs a graph-based local spatial consistency measure to aggregate and embed correspondences, thereby effectively filtering out outliers for robust non-rigid registration. Similarly, GCNNet (Zhu et al., 2022) utilizes GNN to enhance semantic encoding between local regions combined with geometry encodings constructed from the k-NN for multi-level feature extraction. However, while these graph-based methods perform well on surface-to-surface registration tasks, no volume-to-surface registration is discussed, which is essential for accurate vessel tree and tumor registration in liver navigation systems.

Recently, the registration problem in liver navigation has been approached from a 3D-2D formulation where the target is 2D laparoscopic images with hand-crafted or automatically detected features. Given that the segmented source liver model is textureless, only geometrical features can be extracted such as liver ridge, falciform ligament and silhouette based on camera views. Works such as (Robu et al., 2018; Koo et al., 2017; Labrunie et al., 2024) manage to extract corresponding landmarks on 2D images and minimize the discrepancies between 3D and 2D landmarks, achieving rigid or non-rigid registration. Alternatively, approaches like (Collins et al., 2016) enrich the source model with real texture by first aligning intraoperative images with the 3D model, followed by deformable registration based on the deviation in textures and boundaries. The P2ILF challenge (Ali et al., 2025) benchmarks 3D-2D registration by providing a dataset with manually labeled camera poses, where camera pose optimization with differential rendering demonstrates superior performance. Additionally, (Mhiri et al., 2025) proposed a learning-based method that combines 3D synthetic deformation and 2D landmarks to predict intraoperative deformation, yet only patient-specific. One downside of the 3D-2D formulation is that a single view often does not capture enough of the organ. (Espinell et al., 2021) tries to solve this issue by using multiple views. Nevertheless, other limitations such as the inherent ambiguity between 3D models and 2D images, landmarks, hinder the accurate registration between the two.

In this work, we explore a 3D-3D registration algorithm that works directly on volume and surface point clouds, runs at very

high speeds and aims to further enhance registration accuracy in the presence of intraoperative noise and high occlusion, addressing key limitations of existing approaches.

Notably, most of these methods are not set up for the volume-to-surface registration task, or require retraining for application in the surgical domain. However, no available real or phantom dataset contains enough registration pairs for such training, since 3D-3D registration data is very difficult and time-consuming to obtain. Phantom datasets provide the highest number of samples, with 112 registration pairs in the Sparse-DataChallenge dataset (Heiselman et al., 2024) and six pairs in the private phantom dataset presented in section 4.1. Three datasets capture in vivo human liver deformation due to breathing: 3D-IRCADb-02 with one subject and one deformation (irc), the Breathing Motion dataset with two patients and one deformation (Pfeiffer et al., 2020) and the new HHLBM dataset currently comprising seven patients with seven deformed states each 4.1. Intraoperatively, the DePOLL porcine dataset with 12 deformed states of one organ (Modrzejewski et al., 2019) and a clinical dataset with four patients (Rabbani et al., 2022) are available.

In addition to the low number of samples, depending on the original aim of the data collection, only landmarks or sparse correspondences may be available, whereas a dense displacement field is needed for training the volume-to-surface registration task. It has been shown that registration networks can successfully transfer from synthetic training data to applications in the real domain (Pfeiffer et al., 2019, 2020; Ali et al., 2025), which adds the benefit of control over the experimental frame and the possibility to extract any information as needed. Therefore, for this work we also rely on synthetic data for training, generated using the pipeline by Pfeiffer et al. (Pfeiffer et al., 2025), and show that its composition allows for generalization with respect to shapes, intraoperative view, deformation magnitude and noise levels during inference.

3. Methods

Given a preoperative liver volume from MRI / CT, represented by point cloud $\mathbf{V} = \{\mathbf{v}_i \in \mathbb{R}^3 \mid i = 1, \dots, N\}$, and an intraoperative partial liver surface reconstructed from laparoscopic video, noted as point cloud $\mathbf{S} = \{\mathbf{s}_j \in \mathbb{R}^3 \mid j = 1, \dots, M\}$, a non-rigid 3D-3D registration algorithm aims to find a transformation $\mathcal{T} : \mathbb{R}^3 \rightarrow \mathbb{R}^3$ that deforms the source \mathbf{V} to align with the fixed target \mathbf{S} . The deformed $\tilde{\mathbf{V}} = \mathcal{T}(\mathbf{V})$ should reflect the current status of the intraoperative liver. In our case, such a transformation \mathcal{T} can be represented by a 3D displacement field $\Phi \in \mathbb{R}^{N \times 3}$, i.e. $\mathcal{T}(\mathbf{V}) = \mathbf{V} + \Phi$. Our goal is to build a deep network **PIVOTS** which can predict Φ for all points in \mathbf{V} (internal and surface points) directly from the geometry \mathbf{V} and \mathbf{S} , i.e.

$$\Phi = \text{PIVOTS}(\mathbf{V}, \mathbf{S}). \quad (1)$$

Our method adopts a dual-stream encoder-decoder architecture. At the encoder branch, we use farthest point sampling (FPS) and DGCNN (Wang et al., 2019) to iteratively

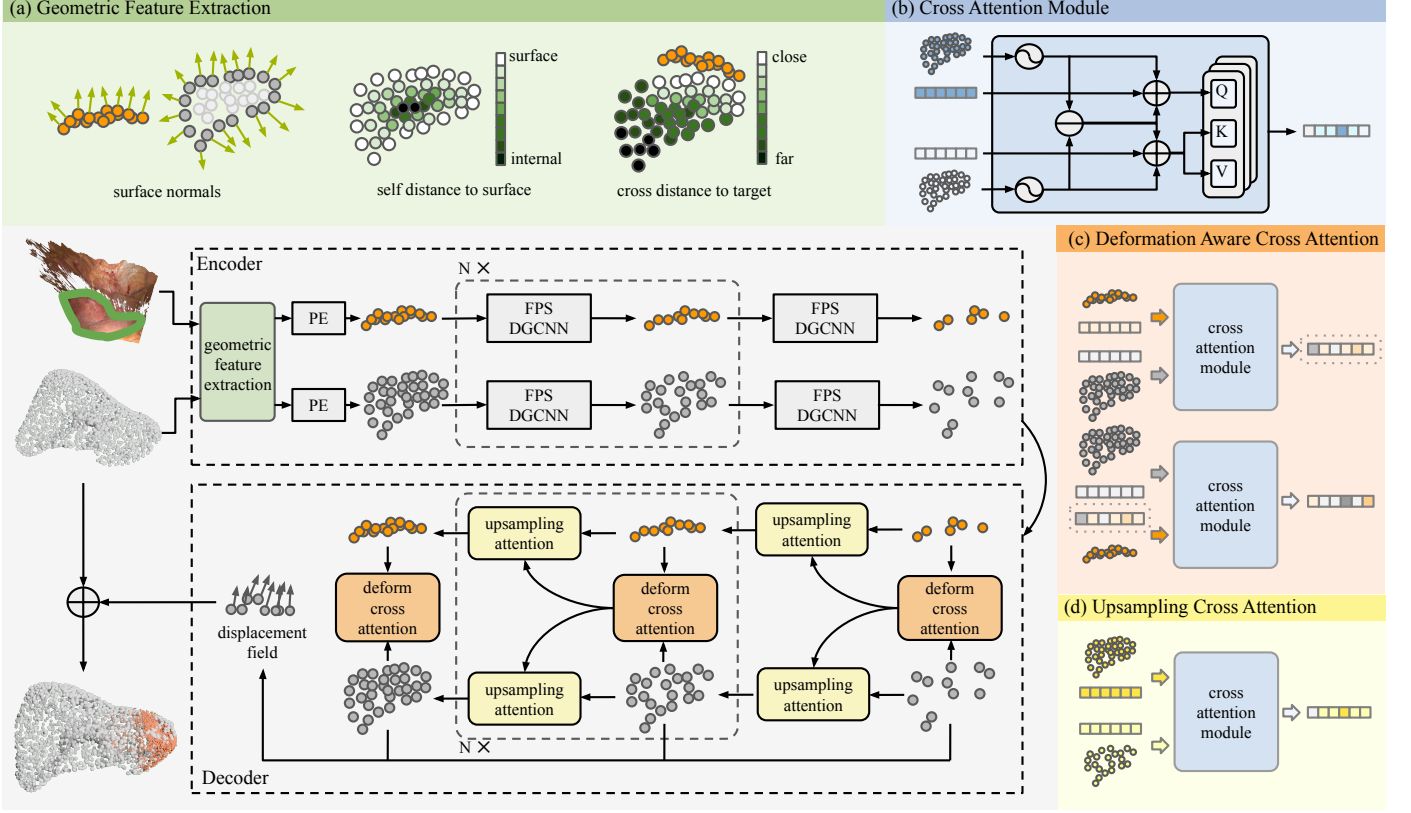


Figure 2: Architecture of the proposed registration network. (a) For the intraoperative target points as well as the surface points of the preoperative point cloud, we encode the surface normals (see Sec. 3.2). For the preoperative source points we additionally encode the smallest distance to the mesh surface as well as the distance to the nearest intraoperative surface point. (b) The point attention module is a core component of the network (described in Sec. 3.3.1). (c) Building upon this attention module, the Deformation Aware Cross Attention combines information from pre- and intraoperative point clouds (see Sec. 3.3.2). (d) The point attention module is also used for the Upsampling Cross Attention module, which propagates features from lower resolutions of the pre- and intraoperative points to higher resolutions (see Sec. 3.3.3). The final network architecture (left) partially resembles a U-Net, with information first being condensed to a lower resolution and then iteratively refined back to the original resolution.

downsample the preoperative and intraoperative point clouds and propagate features at each level. The decoder uses these features to predict the displacement field at each level, using cross-attention to merge information from \mathbf{V} and \mathbf{S} and propagate the merged information between layers. The architecture overview is shown in Fig. 2 and code is available at <https://github.com/pengliu-nct/PIVOTS>. The following will describe all components of the architecture in detail.

3.1. Point Cloud Preprocessor

The original preoperative and intraoperative point clouds are first enhanced by preprocessing steps before being fed into the registration network for deformation prediction. This serves as a standardization scheme for data from various sources and creates additional geometric information which the network can act upon.

First, both pre- and intraoperative meshes are re-sampled to have a common resolution of roughly 5 mm, and several pre-computed features are extracted to help the network understand the geometry of inputs. *Point distance field, F_d* : for each point in the preoperative volume \mathbf{V} , we compute the distance to the closest point in intraoperative surface \mathbf{S} . Likewise, for each point in \mathbf{S} the smallest distance to the surface of \mathbf{V} is computed.

Additionally, for each internal point of \mathbf{V} , we compute its distance to the closest point on the surface. *Surface normals, F_n* : for the surface points in \mathbf{V} and \mathbf{S} , surface normals are computed to help the network identify the orientation of surfaces. *Sinusoidal positional encoding*: for pre- and intraoperative point clouds, sinusoidal positional encodings are computed with 8 frequencies with the mappings: $\xi: \mathbb{R}^3 \rightarrow \mathbb{R}^{6\omega}$, e.g., positional encoding of preoperative points is $\xi_v = [\sin(2^\omega v_i), \cos(2^\omega v_i)]$, where $\omega \in (2^{-1}, 2, 4, 8, 16, 32, \dots)$ is the list of encoding frequencies.

Moreover, to allow batch-processing, both pre- and intraoperative point clouds are further set to exactly n points by either subsampling randomly or by adding dummy points that are way outside the space of interest and ignored during farthest point sampling (FPS). The final inputs to the network are: $\mathbf{V}_r = \{P_v, \xi_v, F_v\}$ and $\mathbf{S}_r = \{P_s, \xi_s, F_s\}$, where $P_v, P_s \in \mathbb{R}^{n \times 3}$, $\xi_s, \xi_v \in \mathbb{R}^{n \times (6\omega)}$ and $F_v, F_s \in \mathbb{R}^{n \times 5}$ (see Fig. 2 (a)). We store all distances and locations in meters.

3.2. Geometric Feature Extraction

Downsampled point clouds no longer retain geometry information compared to original volumes, therefore, we adopt the

widely used DGCNN (Wang et al., 2019) to extract and propagate robust local geometry features between L layers in different resolutions obtained by farthest point sampling (FPS): $(P^{\ell+1}, \xi^{\ell+1}, F^{\ell+1}) = \Pi_{fps}(P^\ell, \xi^\ell, F^\ell, N^\ell)$, where Π_{fps} refers to mapping of FPS function, N^ℓ is the number of points at ℓ -th layer (see a in Fig. 2). Features of next layer $F_v^{\ell+1}, F_s^{\ell+1}$ are updated using two-stream edge convolution for V_r and S_r separately due to the fact that the geometry information of pre- and intraoperative data is naturally different:

$$\hat{F}^{\ell+1} = \max_{j \in \mathcal{K}(i)} \text{ReLu}(\text{MLP}(F_j^\ell - F_i^{\ell+1}, F_i^{\ell+1})) \quad (2)$$

where F^ℓ is features of either preoperative or intraoperative point clouds, \mathcal{K} represents the K nearest neighbors from layer $\ell + 1$ of point i in layer $\ell + 1$, and features are aggregated by the a multi-layer perception MLP, followed by ReLu and maxpool layers.

Using such an encoder constructed by DGCNN and FPS, point clouds are downsampled fast, and the local geometry features are extracted and propagated between layers at different resolutions, which will be refined by the decoder layers for deformation prediction.

3.3. Biomechanical Deformation-aware Transformer

Pre- and intraoperative liver point clouds are orderless and can vary largely in density, shape, and appearance. Thus, it is substantial to design a mechanism that allows features to flow and propagate between the two point cloud pairs in the same or different resolutions. Attention mechanism demonstrates promising performance for point cloud analysis due to its invariance to point order and its ability to enable dynamic information interaction between two arbitrary point clouds. These make the attention mechanism a suitable and efficient analyzer in dealing with pre- and intraoperative point cloud pairs. Therefore, we proposed a novel *Biomechanical Deformation-aware Transformer* consisting of *Deformation Aware Cross Attention* and *Upsampling Cross Attention* modules using *Relative Point Attention* as the core, for pre- and intraoperative point cloud feature interaction and propagation. They are introduced in Sec. 3.3.2 and Sec. 3.3.3.

3.3.1. Relative Point Attention

We propose a *relative point attention* (see b in Fig. 2) which is used in multiple parts of our decoder to compute new features of a *query* point $P_Q \in \mathbb{R}^{N \times 3}$ from its local neighborhood in the target point cloud. We employ vector attention starting with finding the k nearest neighbors $P_K \in \mathbb{R}^{N \times k \times 3}$ of P_Q , which act as the *key* and *value* points. To each feature vector ($F_Q \in \mathbb{R}^{N \times f}$ and $F_{K,k} \in \mathbb{R}^{N \times k \times f}$), we concatenate the point's coordinates both in absolute form and relative to P_Q and P_K , as well as positional encodings ξ (sine and cosines at different frequencies) thereof. We then calculate the query Q , key K and value V vectors as:

$$Q = W_Q(\xi_Q \oplus (\xi_Q \ominus \xi_K) \oplus F_Q) \quad (3)$$

$$K = W_K(\xi_Q \oplus (\xi_Q \ominus \xi_K) \oplus F_{K,k}) \quad (4)$$

$$V = W_V(\xi_Q \oplus (\xi_Q \ominus \xi_K) \oplus F_{K,k}) \quad (5)$$

where $W_q, W_k, W_v \in \mathbb{R}^{c \times f}$ are linear projection matrices, resulting in $Q \in \mathbb{R}^{c \times N}$ and $K, V \in \mathbb{R}^{c \times N \times k}$, $\xi \in \mathbb{R}^{6\omega}$ is sinusoidal positional encoding, here we also include the the positional encoding of the N query points to their k neighbors. F_Q is the point cloud features, and $F_{K,k}$ is the features of the k nearest neighbors of query points. \ominus is an operation for point-wise relative position calculation, and \oplus is a concatenation operation.

Then, attention weights are then calculated using *local additive attention*:

$$\text{att}(Q, K) = \text{Softmax}(\text{MLP}(\tanh(Q + K))) \quad (6)$$

where $\text{att} \in \mathbb{R}^{d \times N \times k}$ is the attention score of Q on K . For each key point, the weighted average of the value features V is computed, resulting in the new features $\tilde{F}_Q \in \mathbb{R}^{d \times N}$ for the query point Q . The query feature F_Q is then the combination of multi-heads of attention modules:

$$\tilde{F}_Q \leftarrow \text{MultiHead}(Q, K, V) = \text{MLP}(\text{cat}[\text{att}_i(Q, K) \cdot V]) \quad (7)$$

where $\tilde{F}_Q \in \mathbb{R}^{N \times d'}$ is the updated query features. In practice, we set the number of attention heads to four.

3.3.2. Deformation Aware Cross Attention

To predict an accurate alignment between the preoperative and intraoperative point clouds, we must allow information to flow between the two clouds. Therefore, based on the proposed local *relative point attention* module, we assemble a *deformation aware cross attention* module (see c in Fig. 2) between preoperative volume points $\mathbf{V}_r^\ell = (P_v^\ell, \xi_v^\ell, F_v^\ell)$ and intraoperative surface points $\mathbf{S}_r^\ell = (P_s^\ell, \xi_s^\ell, F_s^\ell)$ at each resolution ℓ to extract features that are ready to be regressed to predict displacement fields.

The module consists of two cross attention steps. To gain rich information about preoperative points for all intraoperative points, we first employ \mathbf{S}_r^ℓ to attend to \mathbf{V}_r^ℓ :

$$\tilde{F}_s^\ell \leftarrow \text{MultiHead}(Q_s, K_v, V_v) \quad (8)$$

where Q_s is the linearly transformed surface features F_s^ℓ and K_v, V_v come from volume features F_v^ℓ .

With the updated intraoperative surface features being informative of preoperative data, the second attention module is applied, aiming to convey such knowledge to the preoperative point:

$$\tilde{F}_v^\ell \leftarrow \text{MultiHead}(Q_v, \tilde{K}_s, \tilde{V}_s) \quad (9)$$

where \tilde{K}_s, \tilde{V}_s stem from the updated surface features \tilde{F}_s^ℓ , and \tilde{F}_v^ℓ is the updated preoperative features, being aware of the intraoperative points at the current resolution. At this point, information can flow back and forth between the point clouds, and

can propagate between neighborhoods, and F_p^ℓ should contain all necessary information about deformation. Hence, we let the network predict a (downsampled) version of the displacement field Φ^ℓ for every level ℓ :

$$\Phi^\ell = \text{MLP}(\text{ReLU}(F_p)) \quad (10)$$

Such a design enables the information flow in terms of larger deformation between pre- and intraoperative points with the *local additive attention*, as all points from both sides gain the opportunity to update their knowledge regarding their counterparts. We demonstrate the effectiveness in the ablation study in Sec. 4.7.

3.3.3. Upsampling Cross Attention

The abstract features calculated at lower resolutions must later be incorporated back into the features for the higher resolutions in the decoder. For this, *Upsampling Cross Attention* modules (see d in Fig. 2) are built to propagate information from lower layers to higher layers. Taking preoperative volume as an example:

$$\tilde{F}_v^{\ell-1} \leftarrow \text{MLP}(\text{Attn}(F_v^{\ell-1}, F_v^\ell)) \quad (11)$$

where F_v^ℓ (the feature vector at the ℓ -th layer in lower resolution) is used as the key and value vectors and $F_v^{\ell-1}$ (the feature of $(\ell-1)$ -th layer in higher resolution) is used as the query, which will be updated by cross attention to be $\tilde{F}_v^{\ell-1}$. Similar operations are applied between intraoperative points.

3.4. Supervision

At each decoding layer, a displacement field Φ_ℓ is predicted at each layer ℓ , so the total outputs of an L layers network is:

$$\Phi^L = \{\Phi^\ell \in \mathbb{R}^{N \times 3} | \ell = 1, \dots, L\} \quad (12)$$

where Φ^L is the predicted displacement field at the highest resolution.

We train the network in a supervised learning fashion on a synthetic dataset generated using a simulation pipeline (see section 3.5). For each training sample, ground truth displacement field Φ_{gt} is known, so the predicted displacement fields can be compared at each respective resolution using mean squared error (MSE). The total loss function \mathcal{L} is computed as a weighted sum of the losses:

$$\mathcal{L}_{MSE} = \frac{1}{N} \sum_i^N \|\Phi_{gt,i} - \Phi_i\|_2^2 \quad (13)$$

$$\mathcal{L} = \sum_\ell w_\ell \mathcal{L}_{MSE,\ell} \quad (14)$$

where $\Phi_{gt,i}, \Phi_i \in \mathbb{R}^3$ are the predicted and ground truth displacement vectors of a preoperative point. The lower-level losses guide the network to output better features for displacement estimation at high resolution layers, speeding up convergence, while higher-level losses ensure the fidelity and accuracy of the final prediction (Pfeiffer et al., 2020).

3.5. Synthetic Training Data Generation

The synthetic training data generation builds upon a simulation pipeline by (Pfeiffer et al., 2025). Our training data is designed towards providing the network with two core abilities: i) generalizing to new patients without retraining and ii) performing robustly in challenging intraoperative conditions.

Generalization is fostered with respect to organ shape, material and boundary conditions. Diverse, randomly generated organ-like shapes support the adaptation to the natural variation of patients' liver shapes. We try to address the unknown highly variable tissue properties by covering the full range of tissue material parameters. In order to approximate the unknown intraoperative forces which are extremely difficult to measure, like the effects of the pneumoperitoneum, we create a variety of scenarios with differences in magnitude as well as position and surface area which the initial forces act on.

The challenging intraoperative conditions are abstracted as partial views and unavoidable point cloud reconstruction noise. Since it is difficult to encompassingly characterize the different noise properties, we emulate it with a mixture of two noise types in varying strength such that the network can learn to mitigate their effects.

The following sections provide more detail about the training data generation. It starts with the scene setup, implementing the shape variability and placement of boundary conditions, followed by simulating the material's behaviour under the specified forces, extracting a part of the deformed surface and adding noise.

3.5.1. Shape variability

A scene comprises of a deformable object and its surroundings. The liver is represented by a random organ-like shape, created according to a previously published algorithm (Pfeiffer, 2022): A sphere is subjected to several extrusions and subtractions, followed by smoothing. Convex parts reflect the anterior side while concave parts mimic the concavities around the hepatic portal on the posterior side. This results in a shape of roughly the dimensions $d_x = d_y = d_z \sim U(100, 300)$ mm, an example is illustrated in figure 3. Figure 1 in the supplementary material shows the variability of the created shapes alongside two exemplary real livers from the AMOS dataset (Ji et al., 2022), which display the natural variation. In order to create space within the synthetic abdominal cavity, 0 to 3 more organs of the size $d_x = d_y = d_z \sim U(50, 200)$ mm are created additionally. A convex hull spans around these objects with a minimum distance according to $\sim U(0, 50)$ mm, expanded up to 20 mm of Perlin noise along its outward normal, corresponding to a simplified abdominal wall. One or two random paths of up to 100 mm along the deformable organ and extruded towards the abdominal wall imitate ligaments. Finally, a fixed boundary is placed by expanding from a random face of the deformable organ until 2 to 5% of the surface is covered. A comprehensive list of parameters for the scene generation can be found in the supplementary material.

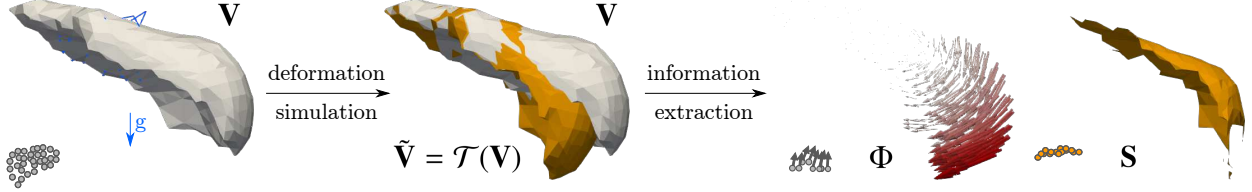


Figure 3: Training data generation. From left to right: Random boundary conditions (blue), including gravity, fixed boundaries (dots) and linear spring boundaries (lines), are placed around a randomly generated organ-like shape with random material properties, representing the preoperative volume \mathbf{V} . Simulation under these conditions leads to a deformed configuration $\tilde{\mathbf{V}}$ (orange) which models the deformation encountered during surgery, e.g. due to tool-tissue interaction. Finally, the ground truth dense displacement field Φ (magnitude-coloured glyphs) and a partial surface with added noise (orange), mimicking an intraoperative point cloud \mathbf{S} reconstructed from the laparoscopic video, can be extracted as training inputs.

3.5.2. Deformation and dense displacement field

Subsequently, the created scene objects are equipped with physical properties. Trying to mimic liver tissue, the deformable organ is modelled as a hyperelastic and nonlinear material with a Young’s modulus $E \sim U(3, 30)$ kPa and a Poisson’s ratio $\nu \sim U(0.45, 0.48)$ informed by literature values (Glozman and Azhari, 2010; Mattei and Ahluwalia, 2016; Marchesseau et al., 2017; Estermann et al., 2020; Lemine et al., 2024), sampled independently in order to cover the parameter space when creating a sufficiently high number of samples. Hyperelasticity is realized using the isotropic compressible Neo-Hookean formulation by Bonet and Wood (Bonet and Wood, 2008) in SOFA’s implementation:

$$\Psi = \frac{\mu}{2}(I_1 - 3) - \mu \ln J + \frac{\lambda}{2}(\ln J)^2$$

$$\text{with } \mu = \frac{E}{2(1 + \nu)}, \lambda = \frac{E}{3(1 - 2\nu)},$$

where Ψ denotes the strain energy, I_1 the first invariant of the right Cauchy-Green tensor and J the Jacobian. For simplification, the material is assumed to be homogeneous with a mass density of $\rho \sim U(1.05, 1.09)$ g/cm³ (Lemine et al., 2024).

The previously created surface is processed into a volumetric tetrahedral mesh using GMSH (Geuzaine and Remacle, 2009) (mesh generation) and the built-in Netgen interface (optimization) (Schöberl et al., 2024), symbolizing the still undeformed, preoperative volume \mathbf{V} . A maximum mesh element size of 1 cm presents a trade-off between accuracy and runtime.

In order to create diverse deformation scenarios we employ three kinds of boundary conditions: Gravity, fixed boundaries and linear elastic springs (blue elements on the left of figure 3). The positions of the latter two have been determined in the scene generation step. The fixed boundaries are enforced as a Dirichlet zero-displacement boundary constraint on the deformable organ’s surface. The spring boundaries between the abdominal wall and the deformable organ’s surface can only move on the organ side. Defined in a state outside of equilibrium, they serve two purposes: In a stretched state, they will pull on the deformable organ, reflecting anatomical ligaments of different strength. In a compressed state, they represent a very simplified version of other organs pushing against the liver. The springs’ initial state is determined by their current length $l = l_0 + \delta l$, the rest length factor $c_0 = \frac{l_0}{l} \sim U(0.9, 1.1)$ to show the deviation from the relaxed state, and the stiffness $k \sim$

$U(100, 300) \frac{\text{N}}{\text{m}}, k = \text{const.}$. Each spring i in a 10 cm ligament object lig is assigned the same k_{lig} and $c_{0,lig}$, with different $\delta l_{lig,i}$ based on the slightly different l due to the initial placement. Each spring’s initial force corresponds to $F_{lig,i} = -k_{lig} \cdot \delta l_{lig,i}$. It follows that $c_0 < 1$ corresponds to a stretched spring (pulling), $c_0 > 1$ to a compressed string (pushing).

The simulation is set up using the SOFA framework (Faure et al., 2012) with an implicit Euler time stepping scheme (step size 50 ms) and a Conjugate Gradient linear system solver. The simulation is run until equilibrium is reached, but in order to obtain higher deformations for training the network, we export the timestep with the highest deformation instead of the final state, therefore including transient dynamic states of the tissue in the training. The difference between the undeformed state \mathbf{V} (grey) and deformed state $\tilde{\mathbf{V}} = \mathcal{T}(\mathbf{V}) = \mathbf{V} + \Phi$ (orange) is illustrated in figure 3, second from the left. Since point correspondences between the undeformed and the deformed mesh stay intact, the ground truth dense displacement field Φ is easily computed, as shown in red colour and magnitude scaled glyphs in figure 3, second from the right.

3.5.3. Intraoperative surfaces

In order to recreate the partial and noisy information of the intraoperatively reconstructed point cloud, a part of the surface of the deformed mesh is extracted and perturbed at random (Pfeiffer, 2022). Starting from a randomly selected mesh vertex as a reference, a randomly weighted sum of the geodesic distance, the angle between the normal vectors and a Poisson noise value is used to select the points to remain. After increasing the number of points on this partial surface by subdivision, an offset is sampled for each direction independently from separate Perlin noise distributions sharing an amplitude A_P , using the point positions as an input $\varepsilon_{x_i} \sim A_P \cdot \text{Perlin}(x_1 \cdot f_{x_i}, x_2 \cdot f_{x_i}, x_3 \cdot f_{x_i}), i \in \{1, 2, 3\}$. Additionally, a Gaussian noise contribution is sampled from $\mathcal{N}(x_i, \sigma)$ for $i \in \{1, 2, 3\}$ and added to the coordinates, followed by a randomized sparsification step to remove few larger areas rather than many small ones. The result is an emulated noisy partial surface \mathbf{S} , visualized in orange in figure 3 (right).

In this manner, after discarding invalid configurations, we create 193,563 samples for training. A full overview of the parameters used in the data generation pipeline can be found in Table 1 in the Supplementary Material.

3.6. Implementation and Training

PIVOTS is implemented in Pytorch and trained on an Nvidia A100 GPU with batch size 20 with a one-cycle learning-rate scheduler (Smith and Topin, 2019) and AdamW optimizer. We use Optuna (Akiba et al., 2019) to fine-tune our hyperparameters with a smaller subsection of the training dataset and then train with the full training dataset and the most promising parameters for 100 epochs. We use $k = 30$ for all neighborhoods in the point attention modules, $e = 29$ for all attention embedding vectors, and all input point clouds are standardized to contain 2,500 points. We build PIVOTS with six down- and upsampling layers ($L = 6$) with [8, 35, 92, 144, 239, 321] points for each downsampled layer respectively, and point feature vectors of length [200, 150, 110, 80, 60, 50] during the downsampling and upsampling stages of the network.

4. Evaluation

We evaluate the proposed network on four datasets, including two synthetic datasets, a phantom dataset, and a real liver dataset, which are introduced in Sec. 4.1. Extensive experiments are conducted to assess the generalizability to various data sources (see Sec. 4.3), robustness against noise (see Sec. 4.5) and varying amounts of surface visibility (see Sec. 4.6). Furthermore, qualitative results are compared to those of many baseline methods (see Sec. 4.8), highlighting the registration qualities of our method.

4.1. Datasets

The **Synthetic** evaluation dataset is generated using the same simulation pipeline described in sec. 3.5 with the same hyperparameters, resulting in a similar deformation and noise distribution, but the samples are unseen during training. This dataset contains 3,008 samples.

The **AMOS** evaluation dataset is a semi-synthetic dataset, where the liver models are reconstructed from labelled real abdominal organ CT scans from the AMOS dataset (Ji et al., 2022) (for details on the data we refer the reader to the original publication) and the deformation is synthetically produced by the same simulation pipeline. 360 livers are selected, which corresponds to the number of scans with publicly available labels, and 3 different sets of boundary conditions are applied to each of the real liver models. Randomly selected noise levels are applied to the random partial surfaces as described above.

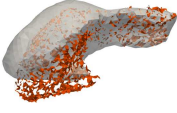
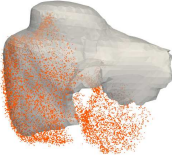
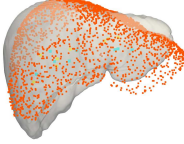
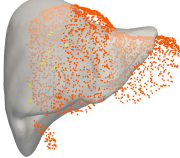
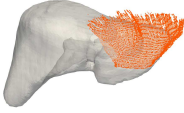
For a thorough evaluation of our method, we additionally create a noise level benchmark on this data, $\text{AMOS}_{\text{noise}}$. For this, in order to imitate a real intraoperative surface more closely, we change the partial surface extraction method of the data generation pipeline to mimic a laparoscopic camera view, and fix a set of constant noise amplitude combinations. The camera view is created by selecting a random position for the camera that remains outside the mesh with a distance of 50 to 200 mm throughout the simulation, setting its focus to a random point of the point cloud and extracting the whole part of the surface that lies within the field of view. The selected fixed noise levels include Perlin noise ranging from $A_p = 0$ mm to $A_p = 15$ mm

with steps of 3 mm and Gaussian noise from $\sigma = 0$ mm to $\sigma = 5$ mm with steps of 2.5 mm. Figure 5 illustrates their effects on the intraoperative surface. This results in 683 samples, each one containing 19 synthetic intraoperative partial surfaces: a random surface with randomly selected noise and one camera view surface for each of the 18 fixed noise levels. An overview of the parameters used to generate the AMOS datasets can be found in Table 2 in the Supplementary Material.

The **Phantom** dataset is acquired from a Kyoto Kagaku abdominal phantom (Zhylyka et al., 2024) (see figure in supplementary) for controlled experiments on real data with complete knowledge of internal deformation. A series of six deformations were applied to the liver using a fake MRI-compatible intraoperative US probe. For each compressed state, an MRI scan was performed (plus one for the uncompressed state). In each case a T2 image was acquired with $\text{TE}=75$ ms, $\text{TR}=5.2$ s, voxel size= $0.88 \times 0.88 \times 3$ mm³ on Philips Ingenia 3.0 T. The phantom was filled with water to avoid artifacts during scanning. To keep the US probe in a fixed position during MRI acquisition, a specialized construction was designed consisting of a rail, fake probe and a holder (see figure in supplementary). All scans were co-registered rigidly via the basin. We marked the same eight landmarks at clearly identifiable positions inside the liver scans in 3D Slicer, using the vessel bifurcations as main guidance. After segmentation of the MRI scans, a partial view of the anterior side of the liver was extracted for each of the six compressed states by simulating the field-of-view of a simple camera. We increased this field of view iteratively (resulting in 20 partial surfaces for each compressed state) and used the uncompressed volume as the preoperative.

The **Healthy Human Liver Breathing Motion (HHLBM)** dataset contains real in vivo liver deformation of healthy subjects during breathing without external disturbance. It enables the evaluation of the proposed network on real human liver deformation. For each healthy subject, data were collected by an MRI scan under three controlled variables: respiratory state (inhaled or exhaled), body posture (supine or prone), and acquisition day (first or second), resulting in a total of eight scan combinations per subject. Images were acquired using a VIBE sequence (T1) with multiple echo acquisitions according to the Dixon method on a Siemens Biograph mMr (3.0 T), voxel size $1.39 \times 1.39 \times 1.5$ mm³. Three annotators are involved in the segmentation process, which consist of one biomedical engineer and two experienced computer scientists. To facilitate the time-consuming manual segmentation process, nnUnetV2 (Isensee et al., 2021) trained on five public liver datasets (LiverHccSeg, Atlas, AMOS, TotalSegmentator MRI, and CHAOS) generates pre-segmentation masks, where only T1-Weighted scans are included to correspond to the focus of the HHLBM dataset. The masks are further refined by the annotators to be the ground truth liver volume. 20 partial surfaces are then extracted from the volumes using the same strategy as for the phantom dataset to reflect intraoperative observations. For landmarks independent of the surface, since no dense correspondence information is available, two annotators search for clearly visible vessel bifurcations and mark their positions in the eight scans. The mean position of the vessel bifurcations is considered the ground truth

Table 1: Comparison of evaluation datasets

	Synthetic	AMOS	Phantom	HHLBM	Laparoscopic
Visualization					
size	3008	690 ($\times 18$ noise)	6 ($\times 20$ targets)	38 ($\times 20$ targets)	6
shape	synthetic	real	phantom	real	real
deformation	synthetic	synthetic	real (tool interaction)	real (breathing, positioning)	real (pneumo-peritoneum, breathing, heartbeat)
metrics	MED	MED	TRE	TRE	-
PRD (mm)	32.14	32.04	17.35	25.78	-

position, and the mean deviation between landmarks from the two annotators is 2.76 mm. Scans with low quality are excluded from the experiments, such as strong artifacts due to the subject moving during the scanning process. For evaluating registration methods, one scan from each patient, the inhaled state in the prone position on the first acquisition day, was designated as the "preoperative" volume \mathbf{V} . The partial surfaces from the other scans of the same patient were chosen as the "intraoperative" partial surfaces \mathbf{S} , the displacement vectors of the corresponding internal landmarks act as a surrogate for the internal displacement field. In total, data from seven subjects was included in the dataset. Overall, this resulted in 38 valid samples for this dataset. The data was collected after obtaining ethics approval (TU Dresden, approval number BO-EK-174042023) and with informed consent from every subject.

The **Laparoscopic** Liver dataset comprises six videos collected from real surgery, i.e., six intraoperative surfaces. The preoperative liver models are segmented from CT scans, and the intraoperative 3D scene is reconstructed from a stereoscopic video recorded from an endoscope during the exploration phase at the beginning of a surgery. Since fully automatic 3D reconstruction methods still struggle with the difficult intraoperative lighting conditions, texture-less surfaces, breathing and heartbeat motion as well as limited visibility, a semi-automatic approach was used to create the intraoperative target surfaces. First, the FoundationStereo method Wen et al. (2025) was used for stereo-reconstruction. From the result, overlapping point clouds were hand-picked and aligned using manually placed point correspondences in the CloudCompare Software. Afterwards, points not belonging to the liver surface were discarded. The result is a point cloud containing a partial view of the intraoperative liver, containing noise from the stereo reconstruction as well as alignment errors due to deformation (See Fig. 8). Patient consent was obtained and the data was collected after approval by the ethics committee (TU Dresden, BO-EK-

137042018).

4.2. Evaluation Metrics

Based on different characteristics of the test sets, we adopt different evaluation metrics. For synthetic and AMOS datasets, ground truth displacement fields are available. Therefore, the mean Euclidean distance (MED) and the root mean squared error (RMSE) are calculated as the dense registration error metric:

$$MED = \frac{1}{N} \sum \|\Phi_{pred} - \Phi_{gt}\|_2 \quad (15)$$

$$RMSE = \left\| \frac{1}{N} \sum (\Phi_{pred} - \Phi_{gt}) \right\|_2 \quad (16)$$

In contrast, phantom and HHLBM datasets, no dense correspondence information is available, so we employ target registration errors (TRE) to evaluate the model performance:

$$TRE = \frac{1}{N} \sum \|\mathcal{T}(L_p) - L_l\|_2 \quad (17)$$

where L_p and L_l are the sparse landmarks in pre- and intraoperative liver volume, $\mathcal{T}(L_p)$ denotes the deformed preoperative landmarks by the estimated displacement field. TRE presents the deviation between the predicted position and actual positions of intraoperative landmarks.

4.3. Comparison with State-of-the-Art Methods

We select widely adopted registration methods from the general computer vision and liver registration communities as our baseline methods. They can be roughly categorized into rigid methods and non-rigid methods. ICP (Besl and McKay, 1992) serves as a rigid, non-learning baseline. GCNNet (Zhu et al., 2022) and LiverMatch (Yang et al., 2023b) are rigid learning-based approaches. Classical non-rigid, non-learning methods include CPD (Myronenko and Song, 2010) and

Table 2: Registration performance comparison between baseline methods across different datasets. Bold face represents the best mean registration error on each dataset, and underlined numbers stand for the second best. If a method increases the registration error compared to the dataset’s PRD, we consider it failed, indicated by a grey font.

Method	Registration Error (mm, Mean \pm SD)			
	Synthetic	AMOS	Phantom	HHLBM
	Samples: 3008 PRD: 32.14	Samples: 683 PRD: 32.04	Samples: 6 PRD: 17.35	Samples: 38 PRD: 25.78
ICP	73.37 \pm 23.77	78.52 \pm 11.84	25.46 \pm 13.99	43.61 \pm 52.26
GCNNNet	23.16 \pm 13.30	26.03 \pm 11.67	32.08 \pm 10.10	31.20 \pm 10.83
LiverMatch	13.94 \pm 13.08	14.57 \pm 12.43	12.33 \pm 3.95	13.45 \pm 2.59
CPD	48.68 \pm 16.50	46.74 \pm 10.84	36.41 \pm 4.61	41.14 \pm 6.45
HMM-CPD	25.53 \pm 15.70	26.31 \pm 15.59	29.44 \pm 3.09	39.40 \pm 9.43
HMM-CPD (aniso)	23.47 \pm 15.27	26.08 \pm 18.68	28.02 \pm 3.02	25.29 \pm 5.23
Robust-DefReg	26.40 \pm 16.10	29.07 \pm 15.44	35.02 \pm 1.45	42.87 \pm 3.20
LiverMatch + NDP	19.60 \pm 18.08	16.60 \pm 12.13	20.12 \pm 2.92	22.34 \pm 3.53
Lepard	19.92 \pm 14.73	21.81 \pm 14.07	16.34 \pm 7.35	19.28 \pm 6.00
C2P-Net	19.15 \pm 13.73	19.17 \pm 12.57	17.00 \pm 1.07	22.21 \pm 4.22
PBSM	27.59 \pm 29.02	30.28 \pm 26.81	10.03 \pm 6.02	8.59 \pm 5.39
BCF_FEM	21.90 \pm 30.47	18.11 \pm 22.49	<u>9.02 \pm 6.34</u>	<u>6.72 \pm 2.88</u>
V2S-Net	<u>6.36 \pm 6.48</u>	<u>6.25 \pm 6.04</u>	9.03 \pm 4.06	7.21 \pm 1.86
PIVOTS (ours)	3.11 \pm 3.38	4.06 \pm 3.35	5.96 \pm 1.47	6.38 \pm 2.56

HMM-CPD (Min et al., 2019, 2020), while PBSM (Suwelack et al., 2014) and BCF_FEM (Yang et al., 2024) represent biomechanics-based non-rigid methods. Learning-based non-rigid methods include Lepard (Li and Harada, 2022a), Robust-DefReg (Monji-Azad et al., 2024), LiverMatch+NDP (Li and Harada, 2022b), C2P-Net (Liu et al., 2024b), and PIVOTS. The hyperparameters of all methods are carefully optimized, and all learning-based methods are trained using the same synthetic training dataset as the proposed method. For PBSM and BCF_FEM, the preoperative surfaces must be meshed with volume elements, which we achieve with the GMSH (Geuzaine and Remacle, 2009) software. Because the speed of these methods strongly depends on the number of elements in the meshes, we downsample surfaces to a maximum of roughly 5000 points.

The results of all methods are listed in Tab. 2, which presents a quantitative comparison of registration performance among a diverse set of baseline methods across four datasets: Synthetic, AMOS, Phantom, and HHLBM. As evaluation metric we use MED computed based on ground truth displacements (Synthetic and AMOS) and TRE calculated from sparse landmarks (Phantom and HHLBM), reported as mean \pm standard deviation in millimeters. For reference, the pre-registration displacement (PRD) is included to indicate the initial misalignment magnitude in each dataset prior to registration.

Overall, the proposed method achieves the lowest mean registration error and Mean + SD across all datasets, outperforming both rigid and non-rigid, traditional and learning-based approaches. Notably, the performance gain is most pronounced in the Synthetic and AMOS datasets, where the average error (3.11 mm and 4.06 mm) is reduced by a substantial margin compared to the next-best methods. In par-

ticular, besides LiverMatch, V2S-Net, and our method, the other methods obtain much worse registration errors around 20 mm and much higher, although learning-based methods are trained on the same dataset and iterative methods are fine-tuned as much as possible. For example, ICP (73.37 mm and 78.52 mm), CPD (48.68 mm and 46.74 mm), and Robust-DefReg (26.40 mm and 29.07 mm) appear to struggle consistently. These results indicate that volume-to-surface registration is a challenging task and requires dedicated designs to tackle the high inconsistency between source and target and accurately infer the movement of internal structures. The comparison between the Synthetic and AMOS datasets also illustrates PIVOTS’ capability to generalize from random shapes during training to real liver shapes at inference time, with an increase in MED from 3.11 \pm 3.38 mm to 4.06 \pm 3.35 mm and RMSE from 4.32 \pm 4.35 mm to 4.96 \pm 4.13 mm, respectively.

Furthermore, on datasets with real deformation, namely the Phantom and HHLBM datasets, our method similarly outperforms others with a registration error of 5.96 mm and 6.38 mm, respectively, suggesting higher robustness and ability of the method in dealing with real noise and deformation compared to baseline methods, e.g., V2S-Net (9.03 mm and 7.21 mm). Beyond absolute performance, the consistency and stability of each method across datasets with various noise and deformation is also critical and significant in practice to ensure safe navigation even when conditions in clinical application may differ. For instance, some methods such as Robust-DefReg and NDP show substantial variation in performance depending on the dataset, suggesting sensitivity to specific deformation characteristics or anatomical context. In contrast, our method demonstrates a stable and low error across all domains, reflecting effective gen-

eralization from synthetic to real anatomical deformation and across different evaluation protocols (dense field vs. sparse landmarks).

In summary, several insights can be obtained:

Volume-to-Surface Registration: For datasets with real deformation, only volume-to-surface baseline methods achieve a registration error lower than 1 cm, e.g. PBSM and V2S-Net, indicating the criticality of volume-to-surface methods in order to obtain high accuracy of the prediction for internal structures. Furthermore, deep learning methods originally designed for surface-to-surface registration, e.g. Leopard and C2P-Net, require dedicated modification to adapt to such a different task in liver navigation.

Necessity of Non-rigid Registration: Although LiverMatch achieves registration errors lower than the majority of non-rigid methods across all four datasets, none of the mean TREs undercut the 1 cm threshold, which is only achieved by four of the nonrigid methods.

Synthetic and Real Domain Gap: Our method obtained a mean registration error lower than 4 mm on datasets with synthetic deformation. However, the performance degrades on the other two real datasets by around 2 mm. This degradation hints at a noticeable gap between synthetic and real datasets, which could be attributed to different materials or properties of the added noise. An alternative influence could be the nature of the deformation: In the synthetic data, the organ can be stretched or folded. The main deformation in the Phantom dataset stems from a US probe causing a local perturbation and the in vivo deformation of the HHLBM dataset is limited by the undisturbed relation of the liver to the surrounding organs and tissues. Especially in later stages of a surgery, one would expect higher deformations than in both of those cases. Therefore, while the performance differences can inform room for improvement in the training data generation, an intraoperative dataset would be highly valuable in assessing the generalization ability to true intraoperative deformations in more detail.

Inference Speed: The methods based on biomechanical simulation (PBSM and BCF_FEM) obtain very good registration results on some samples, especially when hyperparameters are fine-tuned and the initial displacement (PRD) is low. However, they are orders of magnitudes slower and often take more than half a minute for a single sample, while our PIVOTS method roughly takes 230 ms.

4.4. Deformation Level Experiment

Table 3: Pearson and Spearson metrics for Synthetic and AMOS datasets

Method	Synthetic		AMOS	
	Pearson	Spearman	Pearson	Spearman
BCE_FEM	0.437	0.557	0.359	0.561
LiverMatch	0.864	0.904	0.924	0.919
V2S-Net	0.982	0.985	0.981	0.985
ours	0.996	0.995	0.993	0.991

Since the liver undergoes large deformation during surgery, e.g., due to tool manipulation, it is critical for the registration to

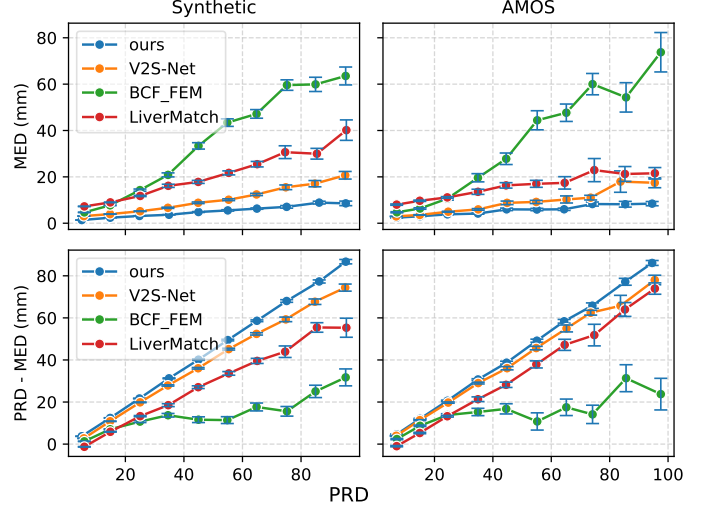


Figure 4: Comparison of methods on various deformation levels (PRD) on the synthetic (left) and AMOS (right) datasets. Top row: Mean Euclidean distance (MED) versus PRD, demonstrating that our method exhibits the greatest robustness to initial misalignment. Bottom row: relative registration error (MED - PRD) versus PRD, showing that our approach achieves the most pronounced error reduction.

reliably capture little as well as highly deformed states. We use the synthetic and AMOS test sets to quantify the influence of different deformation levels on the registration performance of representative methods from each group in Tab. 2 as visualized in Fig. 4. Also, we present the Pearson correlation coefficients in Tab. 3.

From Fig. 4, mean registration errors of our methods increase steadily with a relatively low slope, ending with errors below 10 mm for the largest deformation group (> 80 mm). In comparison, the other baseline methods present a more inclined trend with the increase of the deformation level, especially BCF_FEM, the mean error reaching more than 20 mm for a deformation larger than 40 mm. As a rigid registration method, LiverMatch surpasses BCF_FEM on both test sets and achieves similar errors as V2S-Net when presented with large deformations in the AMOS test set, with an MED of 20 mm.

The relative registration error is computed as $\Delta_{RE} = PRD - MED$, showing how much the registration error increases or decreases compared to the initial error prior to registration. Tab. 3 exhibits different dependencies of relative registration errors on initial error using Pearson correlation coefficients r and Spearman correlation coefficients ρ . Our method achieves near-perfect linear ($r = 0.996$) and rank-order ($\rho = 0.995$) correlations, indicating that larger initial misalignments are almost corrected by proportionally larger amounts. V2S-Net follows closely ($r = 0.981$, $\rho = 0.9850$), likewise demonstrating a very tight coupling between case difficulty and error reduction. In contrast, BCF_FEM shows a substantially weaker relationship ($r = 0.437$, $\rho = 0.557$), reflecting a more equilibrated strategy that yields more uniform improvements regardless of initial error magnitude. As a rigid alignment method, LiverMatch occupies an intermediate position ($r = 0.8643$, $\rho = 0.9043$), balancing targeted correction of challenging cases with non-

negligible gains for easier ones. These results suggest that our method and V2S-Net yield proportional registration error correction, BCF_FEM presents global consistency regardless of the initial misalignment, and LiverMatch shows a comparable capability in error reduction. Overall, our methods exhibit superior performance regarding dealing with both small and large deformations.

4.5. Noise Level Experiments

In 3D-3D liver registration scenarios, the reconstructed liver surfaces using SfM or SLAM from the laparoscopic videos may be corrupted due to various noise or artifacts, substantially degrading the registration accuracy. To quantify the impact of various noise levels, we generated 18 noisy partial surfaces from the AMOS dataset by superimposing Perlin noise (amplitudes $A_P \in \{0, 3, 6, 9, 12, 15\}$ mm) and Gaussian noise ($\sigma \in \{0, 2.5, 5.0\}$ mm) as illustrated in figure 5.

We selected three representative methods with relatively low registration error in Tab. 2 for this experiment, including V2S-Net, BCF_FEM and LiverMatch.

Fig. 6 illustrates all registration results, organized by noise combinations, where the horizontal axis represents Perlin noise and the vertical direction corresponds to Gaussian noise. Overall, PIVOTS maintains a consistently low registration error across all noise combinations, showing strong robustness against various types and amounts of noise. On the other hand, V2S-Net and BCF_FEM present noticeable and rapid degradation with more noise, although the baseline methods work reasonably well with low amounts of noise. In contrast, the errors of PIVOTS show a much steadier deteriorating trend. In particular, the impact of Perlin noise is remarkably larger than Gaussian noise. This finding aligns well with the visualization in Fig. 6, where Gaussian noise makes the partial surface more fuzzy while the basic geometry remains, while on the other hand, target partial surfaces present a bumpy appearance under higher Perlin noise, potentially modifying the geometry and complicating the correspondence exploration for registration methods. These trends are also visible in the qualitative results, illustrated for a subset of the noise levels in Fig. 7: PIVOTS yields stable results with increasing amounts of Gaussian noise and slightly rising errors with higher Perlin noise amplitudes, but the results are qualitatively promising.

Besides the mean error, the development of the error variability further underpins PIVOTS’s strong noise handling capabilities. The top left plot (without noise) shows V2S-Net and PIVOTS clearly outperforming BCF-FEM and LiverMatch while on a similar level to each other. Despite BCF-FEM achieving a mean MED below 1 cm, the error distribution shows roughly a third of samples with an error above this value, making the method unreliable for a considerable subset of patients even in the ideal noise-free setting. With increasing noise levels, the error distribution spreads for all methods in general. However, PIVOTS still manages to contain the error for all but a small fraction of its predictions below the 1 cm threshold even at the highest noise level, giving it a strong edge over the V2S-Net baseline as well.

Additionally, this experiment allows the conclusion that PIVOTS is able to generalize between different surface extraction methods, as it was trained only on randomly extracted surfaces but AMOS_{noise} contains camera-like partial surfaces, and the MED of this experiment remains comparable to the second column of table 2.

4.6. Intraoperative Visibility Experiments

Table 4: TREs (mm) of visibility experiment on the Phantom and HHLBM datasets

Dataset	Vis. Per. (%)	PBSM	BCF_FEM	V2S-Net	ours
Phantom	0 – 10	22.30 ± 6.83	10.22 ± 6.62	13.73 ± 4.88	9.33 ± 4.23
	10 – 20	14.84 ± 6.93	9.32 ± 6.06	9.88 ± 4.43	6.71 ± 2.68
	20 – 30	9.87 ± 5.17	8.89 ± 5.61	8.91 ± 4.18	6.46 ± 1.47
	30 – 40	10.18 ± 5.77	9.49 ± 6.57	9.36 ± 3.99	6.35 ± 1.27
HHLBM	0 – 10	20.56 ± 6.28	18.61 ± 5.67	18.09 ± 7.29	19.93 ± 9.92
	10 – 20	16.04 ± 5.78	13.03 ± 6.43	12.64 ± 6.78	10.25 ± 3.63
	20 – 30	11.01 ± 5.19	8.17 ± 3.72	8.06 ± 2.98	6.95 ± 2.24
	30 – 40	8.89 ± 3.79	7.49 ± 3.07	7.42 ± 2.86	6.04 ± 2.09

Intraoperative liver surfaces are often only partially visible due to limited view angles and occlusion by instruments and adjacent organs, complicating the registration process. We carry out an experiment to examine the performance of the registration methods under various ranges of relative visibility, which is defined as $\alpha = \mathcal{A}(\mathbf{S})/\mathcal{A}(\partial(\mathbf{V}))$, where $\mathcal{A}(\cdot)$ is a function to calculate the area of a given surface, $\partial(\cdot)$ extracts the surface mesh from a volume, and the visibility $\alpha \in [0, 1]$. For this specific experiment we adopt the Phantom and HHLBM test sets. As described in Sec. 4.1, for each sample, both datasets contain 20 partial intraoperative surfaces which are extracted from the view of a virtual camera, observing the anterior side of the liver volumes and gradually moving away from the liver.

For the Phantom dataset, at the most extreme occlusion (0–10% visibility), PBSM yields the largest TRE (22.30 ± 6.83 mm), whereas our method achieves the lowest TRE (9.33 ± 4.23 mm), improving upon V2S-Net by 32% and BCF_FEM by 9% of TRE. As the visibility increases, our method shows a declining trend and always obtains the best TREs around 6.5 mm with a notably lower variability, outperforming BCF_FEM and V2S-Net by 2–3 mm. In comparison, the other methods present a fluctuating trend with the increase of visibility, stagnating around 9 mm TRE.

Regarding TREs on HHLBM dataset, under extreme occlusion (0–10%), V2S-Net and BCF_FEM outperform our method (18.09 mm and 18.61 mm vs. 19.93 mm for our method), suggesting that iterative optimization like BCF_FEM can assist exploration of a better solution and voxelized data like the inputs of V2S-Net favor sensing the ambient small geometry. In contrast, our method performs only one forward end-to-end inference and introduces no extra spatial information. Once over 10% visibility, the TRE of our method drops more quickly than the others and our method outperforms the baseline methods, with around 6 mm as the lowest error at the highest level of visibility. Overall, insights can be drawn from this experiment:

Sensitivity to visibility: All methods benefit from increased visibility (α), but PIVOTS exhibits the steepest decline in TREs,

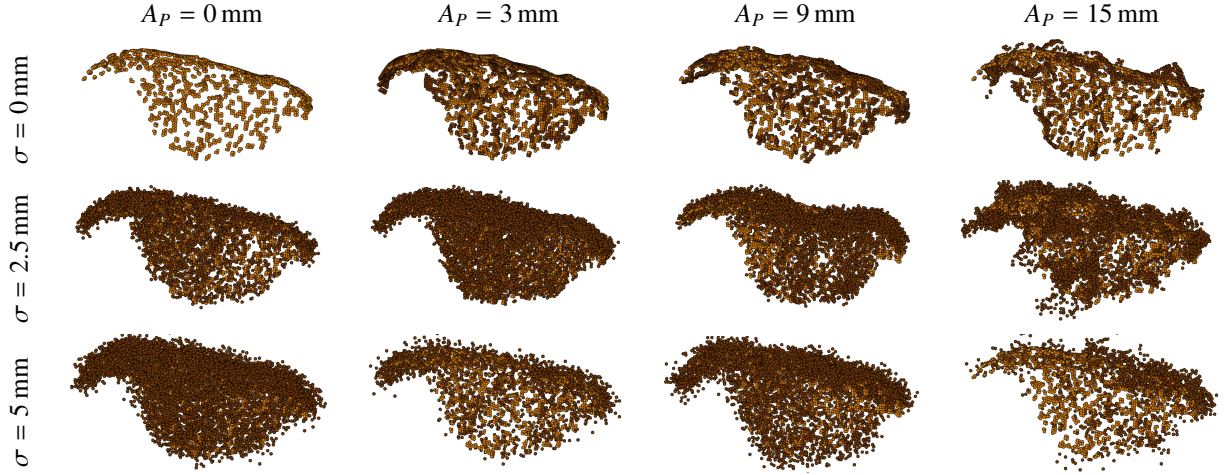


Figure 5: Input for the noise level experiment. Example partial intraoperative surface \mathbf{S} from the $\text{AMOS}_{\text{noise}}$ dataset (orange) with different combinations of Gaussian noise with deviation σ (rows) and Perlin noise with amplitude A_P (columns). Noise levels (brown) increase from left to right and from top to bottom. Gaussian noise blurs the intraoperative point cloud while Perlin noise causes nonuniform local distortions to the apparent surface shape. The randomized subsampling of the point cloud after adding noise additionally increases the difficulty.

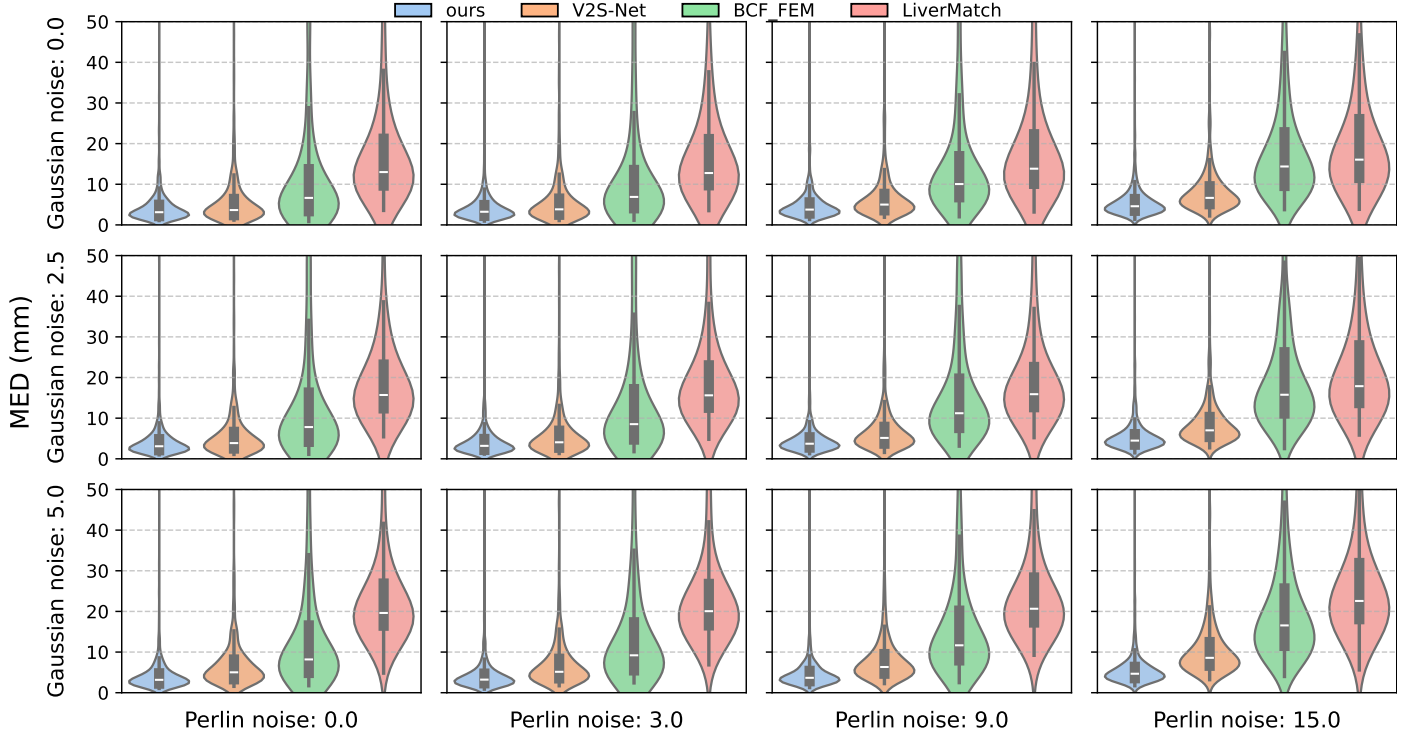


Figure 6: Registration error distributions on various noise levels. Two types of noise are involved: Perlin noise (horizontal, range: $A_P \in \{0, 3, 6, 9, 12, 15\}$ mm) and Gaussian noise (vertical, range: $\sigma \in \{0, 2.5, 5.0\}$ mm). Each subplot exhibits the registration error distribution of four methods. Our method presents the most robustness against various amounts and types of noise.

indicating superior exploitation of additional surface data.

Visibility Threshold: 10% visibility splits the performance of the methods on obtaining TRE lower than 1 cm. But above 10%, methods, especially PIVOTS, rapidly reduce TRE toward less than 7 mm. This indicates a critical visibility threshold that registration methods must aim to tackle for reliable accuracy in clinical setups.

4.7. Ablation Studies

In this section, we investigate various alternative architectures to prove the necessity of the components of our proposed method. For the sake of saving training time, we train all models on a subset of the full generated training set, consisting of around one-third of the samples.

Number of cross-attention layers: We show that increasing the number of layers can increase the registration performance,

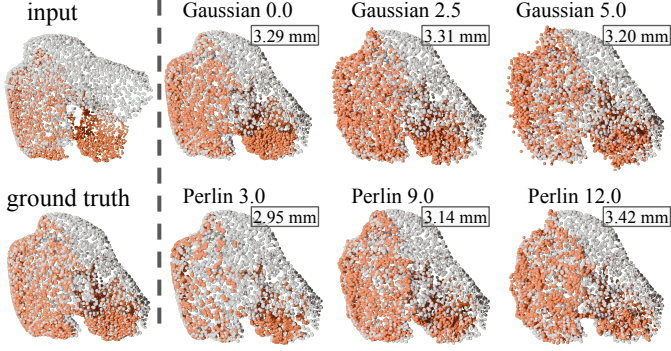


Figure 7: Qualitative comparison between results of PIVOTS on intraoperative surfaces with various Gaussian noise (first row) and Perlin noise amplitudes (second row). The input and ground truth deformation are demonstrated on the left. PIVOTS exhibits strong robustness against various amounts of noise.

Table 5: Ablation study on synthetic dataset

Method	MED (mm)
ours - 2 layers	5.46
ours - 4 layers	4.89
ours w/o deform att	6.60
ours w/o manual features	4.50
ours w/ KPConv encoder	7.01
ours	3.90

however, the gain decreases when more layers are involved, and the training time increases largely. Hence, the chosen number of six layers suits both our hardware setup at hand and registration performance.

Deformation aware cross attention: The counterpart of the proposed deformation aware cross attention is the interweaving attention, where the updated features are fed into cross attention between network layers. The 70% increase in registration error shows the pivotal influence of the deformation aware cross attention modules on the performance of the network, highlighting again the importance of designing the method specifically for this registration task.

Manual feature extraction: We show that without the manually extracted features, the network loses necessary information, so the performance degrades.

KPConv encoder: KPConv works as a successful point cloud encoder for various registration networks, e.g. LiverMatch. In this experiment, the design of kernel points is adopted from KPConv to enrich our encoder. However, despite helping rigid LiverMatch achieve results comparable to non-rigid methods in Tab. 2, the inferior performance in this case proves KPConv is not a suitable component for our architecture.

4.8. Qualitative Results

We visualize registration results of various methods on all test sets in Fig. 8. The first row shows the input point clouds to the method, where the difference of PRDs between the datasets is clearly visible, and the second row contains ground truth for the synthetic and AMOS datasets.

Synthetic data: For the synthetic and AMOS datasets, BCF_FEM and PBSM clearly struggle to accommodate large deformations: their output point clouds remain nearly in the initial pose, indicating a failure to drive the source toward the target geometry. On AMOS in particular, both methods leave the left lobe essentially uncorrected, and BCF_FEM even produces very unrealistic deformation. By contrast, V2S-Net matches the ground-truth displacement well on the synthetic data, but on AMOS its deformation field exhibits abrupt changes. On the other hand, PIVOTS delivers much smoother and coherent displacement fields on both datasets and aligns the source point clouds well with the ground truth, providing an example for its superior quantitative performance.

Real data: For the Phantom and HHLBM samples, surface alignment improves for both BCF-FEM and PBSM relative to the synthetic test sets, aligning well with their gain in quantitative scores on real data in Tab. 2. Nonetheless, none of the two methods fully corrects the Phantom sample’s left-lobe misalignment, and PBSM only slightly outperforms BCF-FEM on the right side. In the HHLBM example, PBSM yields the best result for the surface alignment and the landmarks, especially for the right lobe, and provides a more uniform misalignment vector distribution than V2S-Net. BCF_FEM achieves a good local fit at the center but remains the least effective overall, showing no clear deformation trend. While both V2S-Net and PIVOTS succeed in moving internal landmarks closer to their true positions, PIVOTS exhibits stronger results in both the center / left of the liver and the surface regions.

Intraoperative data: The Laparoscopic Liver dataset allows only qualitative comparison but provides a valuable real intraoperative setting. BCF-FEM yields a plausible close-to-rigid transformation for the majority of the surface but it locally deforms the left lobe of the preoperative surface unrealistically. On the other hand, managing the alignment of the surfaces in the visible region well, only leaving a gap on the leftmost lower part, V2S-Net introduces a strong deformation to the right lobe with a sharp transition without a basis in the intraoperative information. PIVOTS predicts the most coherent deformation without local distortions and matches the partial surface very closely. It also assumes a deformation of the right lobe without a clear indication in the data, however, the displacement is in line with the transformation towards the target area. Since PBSM requires a surface mesh of the intraoperative data and generating such a mesh from the noisy point cloud introduces many additional parameters, highlighting a shortcoming of the method, we exclude it from this experiment.

The qualitative results highlight the ability of PIVOTS to predict consistent displacement fields across various amounts of deformation, while V2S-Net struggles with abrupt field changes and the biomechanical methods tend to introduce unrealistic deformations, especially at a higher discrepancy between source and target.

5. Discussion and Conclusion

Discussion. Our comparison experiment shows that our proposed network not only outperforms biomechanics-based meth-

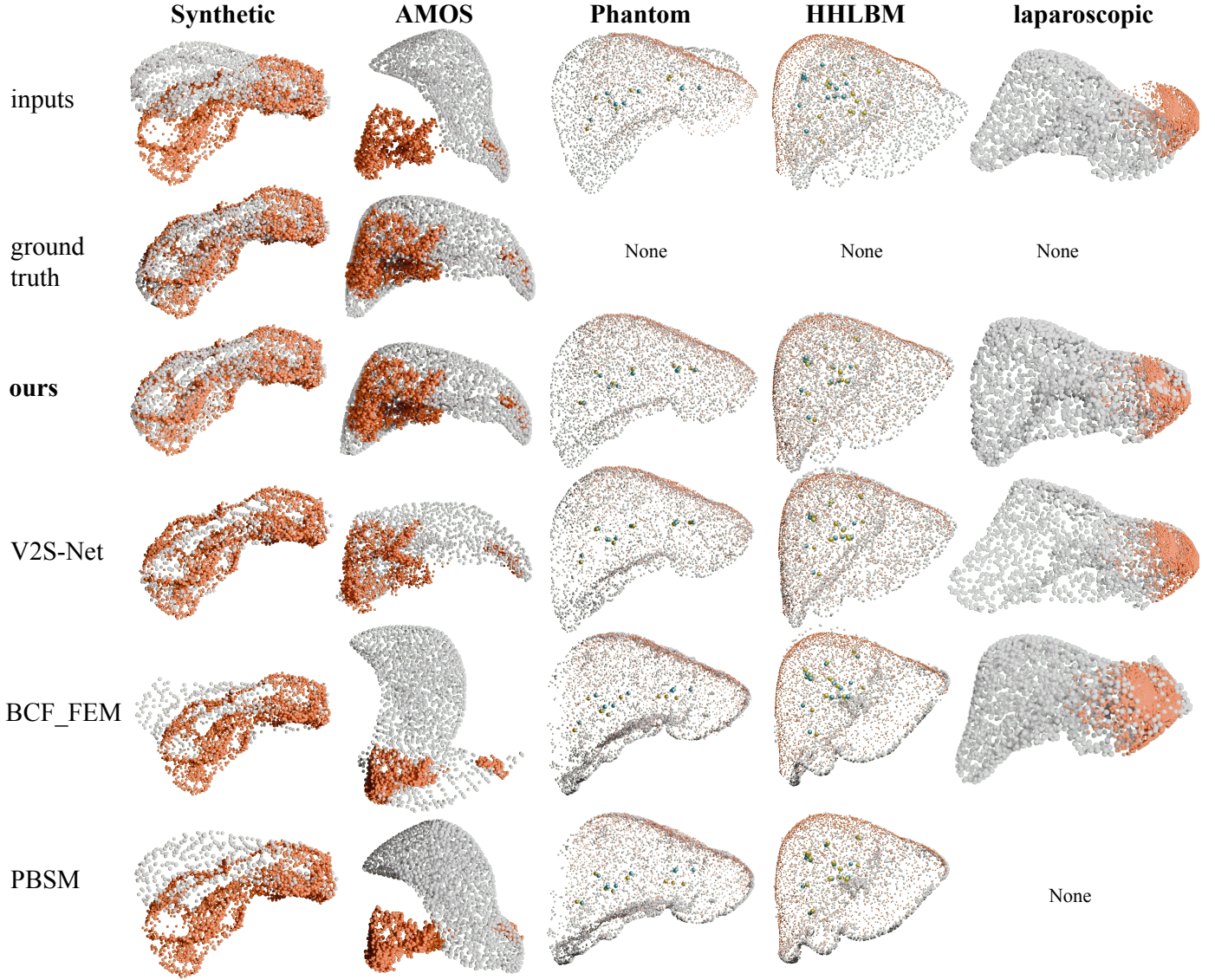


Figure 8: Qualitative comparison on various evaluation datasets. Preoperative point clouds are depicted in **gray**, and intraoperative points in **orange**. For Phantom and HHLBM datasets, preoperative landmarks are shown in **yellow** and intraoperative ones in **blue**. Ground truth information is only available for synthetic and AMOS datasets.

ods like PBSM and BCF_FEM, but also existing deep learning-based methods, e.g. V2S-Net and Leopard, although these methods are re-trained on the same training sets with hyperparameter tuning. Moreover, our method generalizes well across datasets in terms of 1) shape variety: the model trained on synthetic data can seamlessly transfer to inference on AMOS samples, and 2) real datasets: PIVOTS maintains registration errors well below the 1 cm threshold on unseen real-world Phantom and HHLBM datasets, proving its applicability in surgical scenarios.

The robustness of PIVOTS extends to large deformations (0 mm–100 mm PRD), where it achieves less than half the TRE of the next best method and three- to six-fold improvements over other baselines. Its noise resilience is equally impressive: While V2S-Net’s error distribution broadens with increasing perturbation, PIVOTS preserves a tight error profile across both Gaussian and Perlin noise regimes. Furthermore, when faced

with extremely limited fields of view ($< 10\%$ visible surface) on HHLBM samples, our method initially lags behind baseline methods, however, performance rapidly improves with just 10%–20% visibility, achieving less than 1 cm errors across two real datasets. Additionally, PIVOTS exhibits low variability across patients and experimental conditions, ensuring reliable performance not just on average but for every individual case, which is also a critical requirement for clinical deployment.

We attribute this to the dedicated design of the network architecture (proved in the ablation study) and the training data, keeping the special characteristics of the practical surgical application in mind at all times.

Nevertheless, limitations still exist, hindering the translation into the operation room. Our method assumes the availability of a dense intraoperative point cloud. However, real-time 3D reconstruction in the operating room remains challenging. Recent

advances in intraoperative SLAM (Docea et al., 2021), Neural Radiance Fields (NeRFs) for dynamic scenes (Khojasteh et al., 2025), and learning-based deformation tracking (Gong et al., 2024) offer promising directions, but fully robust, low-latency reconstruction pipelines are not yet standard clinical tools.

Like other learning-based 3D–3D non-rigid registration approaches (e.g., V2S-Net), our method presumes an initial rigid alignment of preoperative and intraoperative data. This requirement can limit its applicability in extreme scenarios where only a wrong or no initial pose estimate is available. Future work could integrate a rigid registration module to enable fully end-to-end alignment from arbitrary initial poses.

In our visibility experiments, all methods, including PIVOTS, struggle when less than 10% of the surface is visible. This finding indicates that pipelines for intraoperative surface acquisition must prioritize wide coverage: not only during initial mapping but also through continuous map maintenance, reintegration of temporarily occluded regions, and real-time update of moving structures. Without sufficient coverage, even the most advanced registration networks cannot compensate for missing geometry.

The noticeable sim-to-real gap also calls for further improvements. This could be addressed by creating more realistic synthetic data modelling tool–tissue interaction, self-collision, heterogeneous material properties, volume changes due to pneumoperitoneum, and authentic surgical noise, and the effect of including each aspect would have to be evaluated. Training data efficiency could be increased by exploring adaptive sampling strategies. Gathering high-fidelity intraoperative datasets will be crucial for validating PIVOTS under true clinical conditions.

Finally, even a perfect non-rigid registration of preoperative information onto the intraoperative situation can only visualize what is discernible in the preoperative scan. In many cases, especially small lesions are first detected intraoperatively (Chu et al., 2023; Husarova et al., 2023). Therefore, the further advancement of reliable intraoperative imaging remains indispensable for improved patient outcome, while navigation using non-rigid registration algorithms like PIVOTS aids in contextualizing the resulting captures to transfer them into actionable next steps.

Conclusion. In this work, we propose a point cloud non-rigid liver registration network. This network consists of an encoder with DGCNN and FPS layers, and a decoder with *deformation aware cross attention* and *upsampling cross attention* modules. Through extensive experiments, we demonstrate that the proposed network achieves state-of-the-art performance and outperforms baseline methods on the difficult liver volume-to-surface registration task. Moreover, it presents significant robustness against large deformation, substantial amounts of noise, and various intraoperative visibility, making it a strong candidate for non-rigid registration at the core of an intraoperative navigation system. Finally, in light of the generalizability of our method across random shapes and the easy adaptation of the training data generation to different tissue properties, we trust that the proposed method can be applied in deforma-

tion prediction of many other soft tissues, such as the prostate, lungs, etc.

Future work will focus on improving the registration accuracy on low-visibility surfaces, which could be done by introducing a more powerful point cloud encoder for better geometry information extraction. Another challenging future task is further reducing the sim-to-real domain gap, which can be achieved via more realistic synthetic data generation with surgical scene understanding and dedicated data collection for validation. Additionally, more datasets of other soft tissues can be gathered to evaluate the generalizability of the proposed registration network.

CRedit authorship contribution statement

Peng Liu: Writing – review & editing, Writing – original draft, Visualization, Validation, Resources, Methodology, Investigation, Formal analysis, Data Curation, Conceptualization, Software. **Bianca Güttner:** Writing – review & editing, Writing – original draft, Conceptualization, Software, Validation, Formal analysis, Data Curation, Visualization. **Yutong Su:** Visualization, Data curation, Methodology. **Jinjing Xu:** Writing – review & editing, Visualization. **Chenyang Li:** Writing – review & editing, Visualization. **Mingyang Liu:** Validation, Methodology. **Zhe Min:** Validation, Methodology. **Andrey Zhylka:** Data curation, Resources. **Jasper Smit:** Data curation, Resources. **Karin Olthof:** Data curation, Resources. **Matteo Fusaglia:** Data curation, Resources. **Rudi Apolle:** Data curation, Resources. **Matthias Miederer:** Data curation, Resources. **Laura Frohneberger:** Data curation, Resources. **Carina Riediger:** Conceptualization, Resources. **Jürgen Weitz:** Conceptualization, Resources. **Fiona Kolbinger:** Writing – review & editing, Validation. **Stefanie Speidel:** Writing – review & editing, Validation, Resources, Investigation, Formal analysis, Project administration, Conceptualization, Supervision, Funding acquisition. **Micha Pfeiffer:** Writing – review & editing, Validation, Resources, Investigation, Formal analysis, Project administration, Methodology, Conceptualization, Supervision.

Declaration of competing interest

The authors declare that they have no known competing financial interests or personal relationships that could have appeared to influence the work reported in this paper.

Acknowledgments

This research is funded by the European Union through CloudSkin under grant agreement ID 101092646 and by the German Research Foundation (DFG, Deutsche Forschungsgemeinschaft) as part of Germany’s Excellence Strategy – EXC 2050/1 – Project ID 390696704 – Cluster of Excellence “Centre for Tactile Internet with Human-in-the-Loop” (CeTI) of Technische Universität Dresden.

Data availability

The code and dataset can be accessed from <https://github.com/pengliu-nct/PIVOTS>.

Appendix A. Supplementary material

References

, . Respiratory cycle 3D-IRCADb-02. URL: <https://www.ircad.fr/research/data-sets/respiratory-cycle-3d-ircadb-02/>.

Abu Hilal, M., Aldrighetti, L., Dagher, I., Edwin, B., Troisi, R.I., Alikhanov, R., Aroori, S., Belli, G., Besselink, M., Briceno, J., Gayet, B., D'Hondt, M., Lesurtel, M., Menon, K., Lodge, P., Rotellar, F., Santoyo, J., Scatton, O., Soubrane, O., Sutcliffe, R., Van Dam, R., White, S., Halls, M.C., Cipriani, F., Van Der Poel, M., Ciria, R., Barkhatov, L., Gomez-Luque, Y., Ocana-Garcia, S., Cook, A., Buell, J., Clavien, P.A., Dervenis, C., Fusai, G., Geller, D., Lang, H., Primrose, J., Taylor, M., Van Gulik, T., Wakabayashi, G., Asbun, H., Cherqui, D., 2018. The Southampton Consensus Guidelines for Laparoscopic Liver Surgery: From Indication to Implementation. *Annals of Surgery* 268, 11–18. URL: <https://journals.lww.com/00000658-201807000-00003>, doi:10.1097/SLA.0000000000002524.

Akiba, T., Sano, S., Yanase, T., Ohta, T., Koyama, M., 2019. Optuna: A next-generation hyperparameter optimization framework, in: *Proceedings of the 25th ACM SIGKDD International Conference on Knowledge Discovery and Data Mining*.

Ali, S., Espinel, Y., Jin, Y., Liu, P., Güttner, B., Zhang, X., Zhang, L., Dowrick, T., Clarkson, M.J., Xiao, S., et al., 2025. An objective comparison of methods for augmented reality in laparoscopic liver resection by preoperative-to-intraoperative image fusion from the miccai2022 challenge. *Medical image analysis* 99, 103371.

Amberg, B., Romdhani, S., Vetter, T., 2007. Optimal step nonrigid icp algorithms for surface registration, in: *2007 IEEE conference on computer vision and pattern recognition*, IEEE. pp. 1–8.

Amodu, L.I., Howell, R.S., Daskalaki, D., Allendorf, J.D., 2022. Oncologic benefits of laparoscopic and minimally invasive surgery: a review of the literature. *Annals of Laparoscopic and Endoscopic Surgery* 7, 5–5. URL: <https://ales.amegroups.com/article/view/7382/html>, doi:10.21037/ales-21-19.

Aoki, Y., Goforth, H., Srivatsan, R.A., Lucey, S., 2019. Pointnetlk: Robust & efficient point cloud registration using pointnet, in: *Proceedings of the IEEE/CVF conference on computer vision and pattern recognition*, pp. 7163–7172.

Besl, P., McKay, N.D., 1992. A method for registration of 3-d shapes. *IEEE Transactions on Pattern Analysis and Machine Intelligence* 14, 239–256. doi:10.1109/34.121791.

Bonnet, J., Wood, R.D., 2008. *Nonlinear continuum mechanics for finite element analysis*. 2nd ed ed., Cambridge university press, Cambridge.

Chen, Z., Zou, B., Kui, X., Shi, Y., Lv, D., Chen, L., 2024. Points of interest linear attention network for real-time non-rigid liver volume to surface registration. *Medical Physics* 51, 5351–5360.

Chu, K.J., Kawaguchi, Y., Hasegawa, K., 2023. Current use of intraoperative ultrasound in modern liver surgery. *Oncology and Translational Medicine* 9, 168–175. URL: <https://journals.lww.com/10.1097/ot9.0000000000000005>, doi:10.1097/ot9.0000000000000005.

Collins, T., Bartoli, A., Bourdel, N., Canis, M., 2016. Robust, real-time, dense and deformable 3d organ tracking in laparoscopic videos, in: *International Conference on Medical Image Computing and Computer-Assisted Intervention*, Springer. pp. 404–412.

Docea, R., Pfeiffer, M., Bodenstedt, S., Kolbinger, F.R., Höller, L., Wittig, I., Hoffmann, R.T., Troost, E.G.C., Riediger, C., Weitz, J., Speidel, S., 2021. Simultaneous localisation and mapping for laparoscopic liver navigation : a comparative evaluation study, in: *Linte, C.A., Siewerdsen, J.H. (Eds.), Medical Imaging 2021: Image-Guided Procedures, Robotic Interventions, and Modeling*, International Society for Optics and Photonics. SPIE. p. 115980B. URL: <https://doi.org/10.1117/12.2582121>, doi:10.1117/12.2582121.

Docea, R., Pfeiffer, M., Müller, J., Krug, K., Hardner, M., Riedel, P., Menzel, M., Kolbinger, F.R., Frohneberg, L., Weitz, J., Speidel, S., 2022. A laparoscopic liver navigation pipeline with minimal setup requirements, in: *2022 IEEE Biomedical Circuits and Systems Conference (BioCAS)*, pp. 578–582. doi:10.1109/BioCAS54905.2022.9948587.

Duvenaud, D.K., Maclaurin, D., Iparraguirre, J., Bombarell, R., Hirzel, T., Aspuru-Guzik, A., Adams, R.P., 2015. Convolutional networks on graphs for learning molecular fingerprints. *Advances in neural information processing systems* 28.

Espinel, Y., Calvet, L., Botros, K., Buc, E., Tilmant, C., Bartoli, A., 2021. Using multiple images and contours for deformable 3d-2d registration of a preoperative ct in laparoscopic liver surgery, in: *Medical Image Computing and Computer Assisted Intervention–MICCAI 2021: 24th International Conference, Strasbourg, France, September 27–October 1, 2021, Proceedings, Part IV* 24, Springer. pp. 657–666.

Estermann, S.J., Pahr, D.H., Reisinger, A., 2020. Hyperelastic and viscoelastic characterization of hepatic tissue under uniaxial tension in time and frequency domain. *Journal of the*

- Mechanical Behavior of Biomedical Materials 112, 104038. URL: <https://www.sciencedirect.com/science/article/pii/S1751616120305865?via%3Dihub>, doi:10.1016/j.jmbbm.2020.104038.
- Faure, F., Duriez, C., Delingette, H., Allard, J., Gilles, B., Marchesseau, S., Talbot, H., Courtecuisse, H., Bousquet, G., Peterlik, I., Cotin, S., 2012. SOFA: A Multi-Model Framework for Interactive Physical Simulation, in: Payan, Y. (Ed.), *Soft Tissue Biomechanical Modeling for Computer Assisted Surgery*. Springer. volume 11 of *Studies in Mechanobiology, Tissue Engineering and Biomaterials*, pp. 283–321. doi:10.1007/8415_2012_125.
- Geuzaine, C., Remacle, J., 2009. Gmsh: A 3-D finite element mesh generator with built-in pre- and post-processing facilities. *International Journal for Numerical Methods in Engineering* 79, 1309–1331. doi:10.1002/nme.2579. Version 4.13.1 from 24 May 2024.
- Glozman, T., Azhari, H., 2010. A Method for Characterization of Tissue Elastic Properties Combining Ultrasonic Computed Tomography With Elastography. *Journal of Ultrasound in Medicine* 29, 387–398. URL: <http://doi.wiley.com/10.7863/jum.2010.29.3.387>, doi:10.7863/jum.2010.29.3.387.
- Gojcic, Z., Zhou, C., Wegner, J.D., Wieser, A., 2019. The perfect match: 3d point cloud matching with smoothed densities, in: *Proceedings of the IEEE/CVF conference on computer vision and pattern recognition*, pp. 5545–5554.
- Gong, S., Long, Y., Chen, K., Liu, J., Xiao, Y., Cheng, A., Wang, Z., Dou, Q., 2024. Self-supervised cyclic diffeomorphic mapping for soft tissue deformation recovery in robotic surgery scenes. *IEEE transactions on medical imaging* PP. doi:10.1109/TMI.2024.3439701.
- Guo, Y., Sohel, F., Bennamoun, M., Lu, M., Wan, J., 2013. Rotational projection statistics for 3d local surface description and object recognition. *International journal of computer vision* 105, 63–86.
- Heiselman, J.S., Collins, J.A., Ringel, M.J., Kingham, T.P., Jarnagin, W.R., Miga, M.I., 2024. The Image-to-Physical Liver Registration Sparse Data Challenge: comparison of state-of-the-art using a common dataset. *Journal of Medical Imaging* 11, 015001. URL: <https://doi.org/10.1117/1.JMI.11.1.015001>, doi:10.1117/1.JMI.11.1.015001.
- Hirose, O., 2022. Geodesic-based bayesian coherent point drift. *IEEE transactions on pattern analysis and machine intelligence* 45, 5816–5832.
- Huang, S., Gojcic, Z., Usvyatsov, M., Wieser, A., Schindler, K., 2021. Predator: Registration of 3d point clouds with low overlap, in: *Proceedings of the IEEE/CVF Conference on computer vision and pattern recognition*, pp. 4267–4276.
- Huang, X., Mei, G., Zhang, J., 2020. Feature-metric registration: A fast semi-supervised approach for robust point cloud registration without correspondences, in: *Proceedings of the IEEE/CVF conference on computer vision and pattern recognition*, pp. 11366–11374.
- Husarova, T., MacCuaig, W.M., Dennahy, I.S., Sanderson, E.J., Edil, B.H., Jain, A., Bonds, M.M., McNally, M.W., Menclova, K., Pudil, J., Zaruba, P., Pohnnan, R., Henson, C.E., Grizzle, W.E., McNally, L.R., 2023. Intraoperative Imaging in Hepatopancreatobiliary Surgery. *Cancers* 15, 3694. URL: <https://www.mdpi.com/2072-6694/15/14/3694>, doi:10.3390/cancers15143694.
- Isensee, F., Jaeger, P.F., Kohl, S.A., Petersen, J., Maier-Hein, K.H., 2021. nnu-net: a self-configuring method for deep learning-based biomedical image segmentation. *Nature methods* 18, 203–211.
- Ji, Y., Bai, H., Ge, C., Yang, J., Zhu, Y., Zhang, R., Li, Z., Zhanng, L., Ma, W., Wan, X., et al., 2022. Amos: A large-scale abdominal multi-organ benchmark for versatile medical image segmentation. *Advances in neural information processing systems* 35, 36722–36732.
- Jin, H., Shen, Y., Lou, J., Zhou, K., Zheng, Y., 2024. Keypointdetr: An end-to-end 3d keypoint detector, in: *European Conference on Computer Vision*, Springer. pp. 374–390.
- Khojasteh, S.B., Fuentes-Jimenez, D., Pizarro, D., Espinel, Y., Bartoli, A., 2025. Mis-nerf: neural radiance fields in minimally-invasive surgery. *International Journal of Computer Assisted Radiology and Surgery* URL: <https://doi.org/10.1007/s11548-025-03429-7>, doi:10.1007/s11548-025-03429-7.
- Koo, B., Özgür, E., Le Roy, B., Buc, E., Bartoli, A., 2017. Deformable registration of a preoperative 3d liver volume to a laparoscopy image using contour and shading cues, in: *International conference on medical image computing and computer-assisted intervention*, Springer. pp. 326–334.
- Labrunie, M., Pizarro, D., Tilmant, C., Bartoli, A., 2024. Automatic 3d/2d deformable registration in minimally invasive liver resection using a mesh recovery network, in: Ogu, I., Noble, J., Li, X., Styner, M., Baumgartner, C., Rusu, M., Heinmann, T., Kontos, D., Landman, B., Dawant, B. (Eds.), *Medical Imaging with Deep Learning*, PMLR. pp. 1104–1123. URL: <https://proceedings.mlr.press/v227/labrunie24a.html>.
- Lemine, A.S., Ahmad, Z., Al-Thani, N.J., Hasan, A., Bhadra, J., 2024. Mechanical properties of human hepatic tissues to develop liver-mimicking phantoms for medical applications. *Biomechanics and Modeling in Mechanobiology* 23, 373–396. URL: <https://link.springer.com/10.1007/s10237-023-01785-4>, doi:10.1007/s10237-023-01785-4.

- Li, Y., Harada, T., 2022a. Leopard: Learning partial point cloud matching in rigid and deformable scenes, in: Proceedings of the IEEE/CVF conference on computer vision and pattern recognition, pp. 5554–5564.
- Li, Y., Harada, T., 2022b. Non-rigid point cloud registration with neural deformation pyramid. *Advances in Neural Information Processing Systems* 35, 27757–27768.
- Liu, P., Bodenstedt, S., Kolbinger, F., Riediger, C., Weitz, J., Speidel, S., Pfeiffer, M., 2024a. Leveraging expert knowledge for real-time online adaptation of intraoperative liver registration, in: *International Workshop on Shape in Medical Imaging*, Springer. pp. 137–148.
- Liu, P., Golde, J., Morgenstern, J., Bodenstedt, S., Li, C., Hu, Y., Chen, Z., Koch, E., Neudert, M., Speidel, S., 2024b. Non-rigid point cloud registration for middle ear diagnostics with endoscopic optical coherence tomography. *International Journal of Computer Assisted Radiology and Surgery* 19, 139–145.
- Marchesseau, S., Chatelin, S., Delingette, H., 2017. Nonlinear Biomechanical Model of the Liver, in: *Biomechanics of Living Organs*. Elsevier, pp. 243–265. URL: <https://linkinghub.elsevier.com/retrieve/pii/B9780128040096000110>, doi:10.1016/B978-0-12-804009-6.00011-0.
- Mattei, G., Ahluwalia, A., 2016. Sample, testing and analysis variables affecting liver mechanical properties: A review. *Acta Biomaterialia* 45, 60–71. URL: <https://linkinghub.elsevier.com/retrieve/pii/S1742706116304603>, doi:10.1016/j.actbio.2016.08.055.
- Mhiri, I., Pizarro, D., Bartoli, A., 2025. Neural patient-specific 3d–2d registration in laparoscopic liver resection. *International Journal of Computer Assisted Radiology and Surgery* 20, 57–64.
- Min, Z., Liu, L., Meng, M.Q.H., 2019. Generalized non-rigid point set registration with hybrid mixture models considering anisotropic positional uncertainties, in: *Medical Image Computing and Computer Assisted Intervention–MICCAI 2019: 22nd International Conference, Shenzhen, China, October 13–17, 2019, Proceedings, Part V 22*, Springer. pp. 547–555.
- Min, Z., Zhu, D., Ren, H., Meng, M.Q.H., 2020. Feature-guided nonrigid 3-d point set registration framework for image-guided liver surgery: From isotropic positional noise to anisotropic positional noise. *IEEE Transactions on Automation Science and Engineering* 18, 471–483.
- Modrzejewski, R., Collins, T., Seeliger, B., Bartoli, A., Hostettler, A., Marescaux, J., 2019. An in vivo porcine dataset and evaluation methodology to measure soft-body laparoscopic liver registration accuracy with an extended algorithm that handles collisions. *International Journal of Computer Assisted Radiology and Surgery* 14, 1237–1245. URL: <http://link.springer.com/10.1007/s11548-019-02001-4>, doi:10.1007/s11548-019-02001-4.
- Monji-Azad, S., Kinz, M., Männel, D., Scherl, C., Hesser, J., 2024. Robust-defreg: a robust coarse to fine non-rigid point cloud registration method based on graph convolutional neural networks. *Measurement Science and Technology* 36, 015426.
- Murad Gutiérrez, V., Romero Enciso, J., 2018. Liver elastography: What it is, how it is done, and how it is interpreted. *Radiología (English Edition)* 60, 183–189. URL: <https://linkinghub.elsevier.com/retrieve/pii/S217351071830020X>, doi:10.1016/j.rxeng.2018.03.003.
- Myronenko, A., Song, X., 2010. Point set registration: Coherent point drift. *IEEE transactions on pattern analysis and machine intelligence* 32, 2262–2275.
- Nguyen, K.T., Marsh, J.W., Tsung, A., Steel, J.J.L., Gamblin, T.C., Geller, D.A., 2011. Comparative benefits of laparoscopic vs open hepatic resection: a critical appraisal. *Archives of surgery* 146, 348–356.
- Novitsky, Y.W., Litwin, D.E.M., Callery, M.P., 2004. The net immunologic advantage of laparoscopic surgery. *Surgical Endoscopy* 18, 1411–1419. URL: <http://link.springer.com/10.1007/s00464-003-8275-x>, doi:10.1007/s00464-003-8275-x.
- Özgür, E., Koo, B., Le Roy, B., Buc, E., Bartoli, A., 2018. Preoperative liver registration for augmented monocular laparoscopy using backward–forward biomechanical simulation. *International journal of computer assisted radiology and surgery* 13, 1629–1640.
- Pfeiffer, M., 2022. Non-Rigid Liver Registration for Laparoscopy using Data-Driven Biomechanical Models. Dissertation. Technische Universität Dresden. Dresden, Germany. URL: <https://nbn-resolving.org/urn:nbn:de:bsz:14-qucosa2-793702>.
- Pfeiffer, M., Güttner, B., Liu, P., Tagliabue, E., Fiorini, P., Speidel, S., 2025. Open-source synthetic organ simulation pipeline for laparoscopic navigation applications, in: *The 16th International Conference on Information Processing in Computer-Assisted Interventions*. Accepted as Long Abstract to appear at IPCAI Conference, Berlin, Germany, June 2025.
- Pfeiffer, M., Riediger, C., Leger, S., Kühn, J.P., Seppelt, D., Hoffmann, R.T., Weitz, J., Speidel, S., 2020. Non-rigid volume to surface registration using a data-driven biomechanical model, in: Martel, A.L., Abolmaesumi, P., Stoyanov, D., Mateus, D., Zuluaga, M.A., Zhou, S.K., Racoceanu, D., Joskowicz, L. (Eds.), *Medical Image Computing and Computer Assisted Intervention – MICCAI 2020*, Springer International Publishing, Cham. pp. 724–734.

- Pfeiffer, M., Riediger, C., Weitz, J., Speidel, S., 2019. Learning soft tissue behavior of organs for surgical navigation with convolutional neural networks. *International Journal of Computer Assisted Radiology and Surgery* 14, 1147–1155. URL: <http://link.springer.com/10.1007/s11548-019-01965-7>, doi:10.1007/s11548-019-01965-7.
- Qi, C.R., Su, H., Mo, K., Guibas, L.J., 2017a. Pointnet: Deep learning on point sets for 3d classification and segmentation, in: *Proceedings of the IEEE conference on computer vision and pattern recognition*, pp. 652–660.
- Qi, C.R., Yi, L., Su, H., Guibas, L.J., 2017b. PointNet++: Deep Hierarchical Feature Learning on Point Sets in a Metric Space, in: *Advances in Neural Information Processing Systems*.
- Qin, Z., Yu, H., Wang, C., Guo, Y., Peng, Y., Ilic, S., Hu, D., Xu, K., 2023a. Geotransformer: Fast and robust point cloud registration with geometric transformer. *IEEE Transactions on Pattern Analysis and Machine Intelligence* 45, 9806–9821.
- Qin, Z., Yu, H., Wang, C., Peng, Y., Xu, K., 2023b. Deep graph-based spatial consistency for robust non-rigid point cloud registration, in: *Proceedings of the IEEE/CVF Conference on Computer Vision and Pattern Recognition*, pp. 5394–5403.
- Rabbani, N., Calvet, L., Espinel, Y., Le Roy, B., Ribeiro, M., Buc, E., Bartoli, A., 2022. A methodology and clinical dataset with ground-truth to evaluate registration accuracy quantitatively in computer-assisted Laparoscopic Liver Resection. *Computer Methods in Biomechanics and Biomedical Engineering: Imaging & Visualization* 10, 441–450. URL: <https://www.tandfonline.com/doi/full/10.1080/21681163.2021.1997642>, doi:10.1080/21681163.2021.1997642.
- Ratti, F., Fiorentini, G., Cipriani, F., Catena, M., Paganelli, M., Aldrighetti, L., 2018. Laparoscopic vs open surgery for colorectal liver metastases. *JAMA surgery* 153, 1028–1035.
- Robu, M.R., Ramalhinho, J., Thompson, S., Gurusamy, K., Davidson, B., Hawkes, D., Stoyanov, D., Clarkson, M.J., 2018. Global rigid registration of ct to video in laparoscopic liver surgery. *International Journal of Computer Assisted Radiology and Surgery* 13, 947–956.
- Rodola, E., Albarelli, A., Bergamasco, F., Torsello, A., 2013. A scale independent selection process for 3d object recognition in cluttered scenes. *International journal of computer vision* 102, 129–145.
- Rusu, R.B., Blodow, N., Beetz, M., 2009. Fast point feature histograms (fpfh) for 3d registration, in: *2009 IEEE international conference on robotics and automation*, IEEE. pp. 3212–3217.
- Rusu, R.B., Blodow, N., Marton, Z.C., Beetz, M., 2008. Aligning point cloud views using persistent feature histograms, in: *2008 IEEE/RSJ international conference on intelligent robots and systems*, IEEE. pp. 3384–3391.
- Santhosh, I., Yadav, T., Garg, S., Kumar, K., Singh, H., Kurdia, K., 2024. Study of variations in the biliary anatomy of the liver (extra and intrahepatic biliary apparatus)-a study of 100 cadaveric liver dissection in a tertiary care center. *HPB* 26, S263–S264.
- Sarode, V., Li, X., Goforth, H., Aoki, Y., Srivatsan, R.A., Lucey, S., Choset, H., 2019. Pcnnet: Point cloud registration network using pointnet encoding. *arXiv preprint arXiv:1908.07906*.
- Scarselli, F., Gori, M., Tsoi, A.C., Hagenbuchner, M., Monfardini, G., 2008. The graph neural network model. *IEEE transactions on neural networks* 20, 61–80.
- Schöberl, J., Lackner, C., Hochsteger, M., Dorigo, R., Hirschschall, S., Leonhartsberger, C., 2024. Netgen/NGSolve. <https://ngsolve.org/>. URL: <https://netgen-mesher.svn.sourceforge.net/svnroot/netgen-mesher.svn> revision 469 from 1 December 2011 with changes as stated in GMSH source.
- Shi, J., Wan, P., Chen, F., 2021. An unsupervised non-rigid registration network for fast medical shape alignment, in: *2021 43rd Annual International Conference of the IEEE Engineering in Medicine & Biology Society (EMBC)*, IEEE. pp. 1887–1890.
- Singh, H.R., Rabi, S., 2019. Study of morphological variations of liver in human. *Translational research in Anatomy* 14, 1–5.
- Sipiran, I., Bustos, B., 2011. Harris 3d: a robust extension of the harris operator for interest point detection on 3d meshes. *The Visual Computer* 27, 963–976.
- Smith, L.N., Topin, N., 2019. Super-convergence: very fast training of neural networks using large learning rates, in: *Pham, T. (Ed.), Artificial Intelligence and Machine Learning for Multi-Domain Operations Applications*, International Society for Optics and Photonics. SPIE. p. 1100612. URL: <https://doi.org/10.1117/12.2520589>, doi:10.1117/12.2520589.
- Srimani, P., Saha, A., 2020. Liver morphology: anatomical study about the outer aspects. *Surgical and Radiologic Anatomy* 42, 1425–1434.
- Streiff, D., Bernreiter, L., Tschopp, F., Fehr, M., Siegwart, R., 2021. 3d3l: Deep learned 3d keypoint detection and description for lidars, in: *2021 IEEE International Conference on Robotics and Automation (ICRA)*, IEEE. pp. 13064–13070.
- Suwelack, S., Röhl, S., Bodenstedt, S., Reichard, D., Dillmann, R., dos Santos, T., Maier-Hein, L., Wagner, M., Wünscher, J., Kennigott, H., et al., 2014. Physics-based shape matching for intraoperative image guidance. *Medical physics* 41, 111901.

- Thomas, H., Qi, C.R., Deschaud, J.E., Marcotegui, B., Goulette, F., Guibas, L.J., 2019. Kpconv: Flexible and deformable convolution for point clouds, in: Proceedings of the IEEE/CVF international conference on computer vision, pp. 6411–6420.
- Tombari, F., Di Stefano, L., 2010. Object recognition in 3d scenes with occlusions and clutter by hough voting, in: 2010 Fourth Pacific-Rim Symposium on Image and Video Technology, IEEE. pp. 349–355.
- Wang, Y., Solomon, J.M., 2019. Deep closest point: Learning representations for point cloud registration, in: Proceedings of the IEEE/CVF international conference on computer vision, pp. 3523–3532.
- Wang, Y., Sun, Y., Liu, Z., Sarma, S.E., Bronstein, M.M., Solomon, J.M., 2019. Dynamic graph cnn for learning on point clouds. *ACM Transactions on Graphics (tog)* 38, 1–12.
- Wen, B., Treppe, M., Aribido, J., Kautz, J., Gallo, O., Birchfield, S., 2025. Foundationstereo: Zero-shot stereo matching. *CVPR*.
- Yang, J., Li, H., Campbell, D., Jia, Y., 2015. Go-icp: A globally optimal solution to 3d icp point-set registration. *IEEE transactions on pattern analysis and machine intelligence* 38, 2241–2254.
- Yang, J., Zhang, X., Fan, S., Ren, C., Zhang, Y., 2023a. Mutual voting for ranking 3d correspondences. *IEEE Transactions on Pattern Analysis and Machine Intelligence*.
- Yang, Z., Simon, R., Linte, C.A., 2023b. Learning feature descriptors for pre-and intra-operative point cloud matching for laparoscopic liver registration. *International journal of computer assisted radiology and surgery* 18, 1025–1032.
- Yang, Z., Simon, R.A., Merrell, K., Linte, C.A., 2024. Boundary constraint-free biomechanical model-based surface matching for intraoperative liver deformation correction. *IEEE Transactions on Medical Imaging* 44, 1723–1734. URL: <https://api.semanticscholar.org/CorpusID:268510028>.
- Yew, Z.J., Lee, G.H., 2022. Regtr: End-to-end point cloud correspondences with transformers, in: Proceedings of the IEEE/CVF conference on computer vision and pattern recognition, pp. 6677–6686.
- Zeng, A., Song, S., Nießner, M., Fisher, M., Xiao, J., Funkhouser, T., 2017. 3dmatch: Learning local geometric descriptors from rgb-d reconstructions, in: Proceedings of the IEEE conference on computer vision and pattern recognition, pp. 1802–1811.
- Zhao, H., Jiang, L., Jia, J., Torr, P.H., Koltun, V., 2021. Point transformer, in: Proceedings of the IEEE/CVF International Conference on Computer Vision (ICCV), pp. 16259–16268.
- Zhao, X., Wu, X., Miao, J., Chen, W., Chen, P.C., Li, Z., 2022. Alike: Accurate and lightweight keypoint detection and descriptor extraction. *IEEE Transactions on Multimedia* 25, 3101–3112.
- Zhu, L., Guan, H., Lin, C., Han, R., 2022. Neighborhood-aware geometric encoding network for point cloud registration. *arXiv preprint arXiv:2201.12094* 4.
- Zhylyka, A., Smit, J., Olthof, K., ter Beek, L., Ruers, T., Fusaglia, M., 2024. Simulated liver deformations with intraoperative ultrasound: steps towards a multi-modal dataset. *International Journal of Computer Assisted Radiology and Surgery* 19, 135–136. doi:10.1007/s11548-024-03128-9. computer Assisted Radiology and Surgery 2024, CARS ; Conference date: 18-06-2024 Through 21-06-2024.

1. Supplementary Material

1.1. Shape variability in generated training data

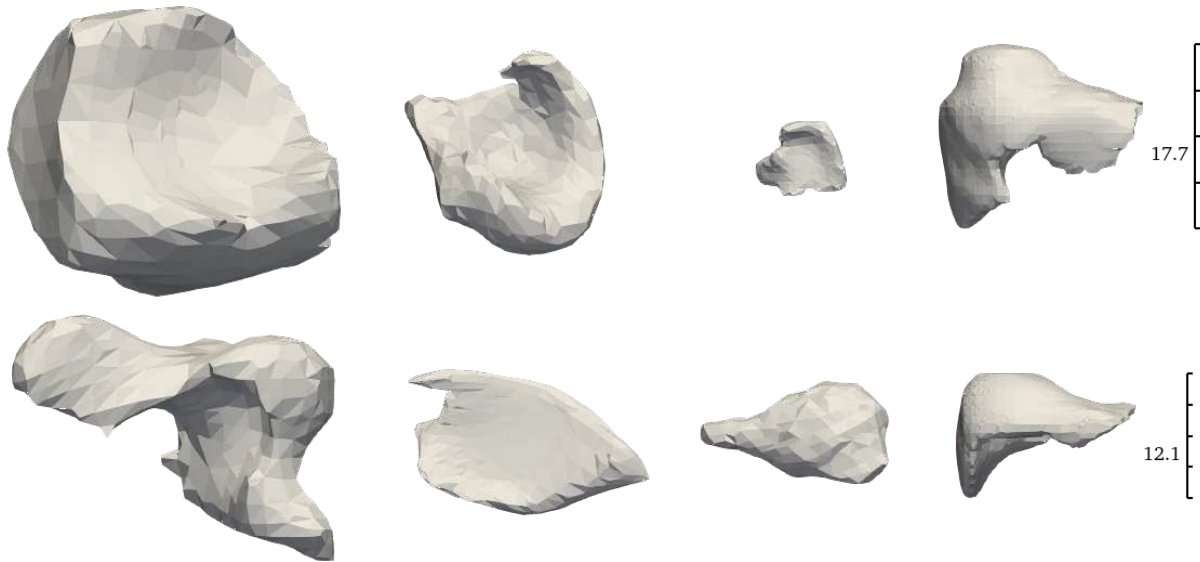


Figure 1: Shape variation in training data alongside two exemplary real livers. Left: synthetic shapes, upper row: examples for different sizes, bottom row: examples for different shapes: concave, flat, and liver-like. Right: real livers (AMOS) and their variability. Bounding rulers show the liver size in superior-inferior direction in cm, all shapes shown in correct size relation.

1.2. Data generation parameters

Table 1: Parameters used in the generation of the synthetic training data.

Pipeline block or scene object	Parameter	Value or range
Deformable organ	Young's modulus E	$U(3, 30)$ kPa
	Poisson ratio η	$U(0.45, 0.48)$
	mass density ρ	$U(1050, 1090) \frac{\text{kg}}{\text{m}^3}$
	size	$U(0.1, 0.3)$ m
	create concavities	True
	predeform twist	True
	predeform noise	True
	cut to fit	True
	voxel resolution	1 m

Continued on next page

Pipeline block or scene object	Parameter	Value or range
Organ placeholders	size	$U(0.05, 0.2)$ m
	existence likelihood	0.9 for $i < 1$, 0.5 otherwise,
	create concavities	$0 \leq i \leq 2$ $P(\text{True}) = 0.5$
Ligaments	existence likelihood	1 for $i = 0$, 0.3 otherwise,
		$0 \leq i \leq 1$
	stiffness k_{lig}	$U(100, 300) \frac{\text{N}}{\text{m}}$
	rest length factor c_0	$U(0.9, 1.1)$
Fixed attachments	path length	0.1 m
	surface amount	$U(2, 5)\%$
Abdominal wall	base outset amount	$U(0, 0.05)$ m
	outset noise amplitude	$U(0, 0.02)$ m
	outset noise frequency	$U(1, 10)$
Random scene block	extrusion size factor for deformable organ	0.5
	target minimum voxel size (blender)	0.02 m
GMSH meshing block	maximum mesh element size	0.01 m
Simulation block	time step	50 ms
	linear system solver	Conjugate Gradient
	maximum iterations	1000
	minimum threshold	10^{-8}
	tolerance	10^{-8}
	time stepping scheme	Implicit Euler
	Rayleigh damping stiffness coefficient	0.1
	Rayleigh damping mass coefficient	0.1
Random surface extraction block	surface amount	$U(10, 100)\%$
	noise frequency	15 in x, y and z direction
	noise phase	$U(0, 150)$ in x, y and z direction
	geodesic distance weight	$U(0.1, 1)$
	surface normal alignment weight	$U(0.1, 1)$
	noise weight	$U(0.1, 1)$
Camera view surface extraction block	mesh distance	$U(0.05, 0.2)$ m
	window width	$U(0.03, 0.1)$ m
	aspect ratio	$P(16/9) = P(4/3) = 0.5$
	horizontal view angle	70°

Continued on next page

Pipeline block or scene object	Parameter	Value or range
Surface noise block	Perlin noise amplitude A_P	$U(0, 0.01)$ m
	Perlin noise frequency	$U(10, 70)$ in x, y and z direction
	Perlin noise phase	$U(1, 999)$
	Gaussian noise σ	$U(0, 0.003)$ m
	subdivision factor	$U(5, 15)$
	maximum subdivision triangle area	10^{-5}
	maximum subdivision edge length	10^{-5}
	sparsification Perlin noise frequency	$U(1, 5)$
	sparsification scale	1
	sparsification shift	-0.3

Table 2: Parameters used in the generation of the AMOS validation and the AMOS_{noise} data. Only parameters are listed that differ from the training data generation. Surface noise for the AMOS validation set was created as listed in table 1 for the training data, for AMOS_{noise} please refer to this table.

Pipeline block or scene object	Parameter	Value or range
Ligaments	rest length factor c_0	$U(0.7, 1.1)$
Scene object generator block	source mesh scale factor	10^{-3}
Random scene block	blender remeshing octree depth	5
	blender remeshing scale	0.75
	mesh subdivision	False
	remove non-manifold regions	True
Surface noise block	Perlin noise amplitude A_P	$\in \{0, 3, 6, 9, 12, 15\}$ mm
	Gaussian noise σ	$\in \{0, 2.5, 5\}$ mm

1.3. Phantom test dataset collection

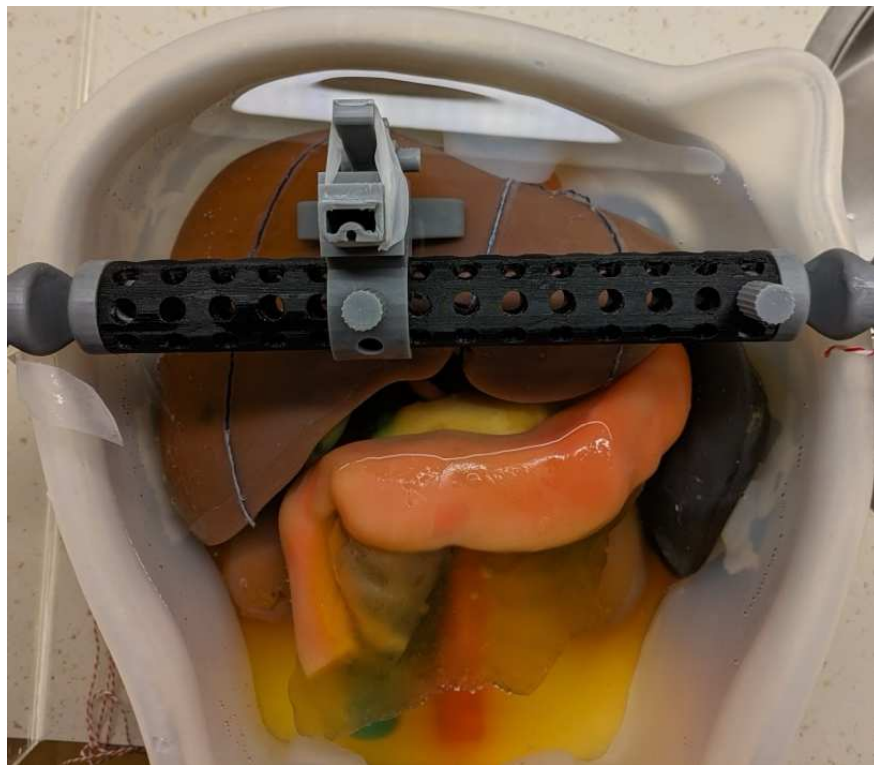


Figure 2: Phantom setup before MRI acquisition. The rail allows to fix the fake US probe and maintain the deformation during the scan.